Annexin A1 is a polarity cue that directs planar mitotic spindle orientation during mammalian epithelial morphogenesis

Maria Fankhaenel[1,2], Farahnaz Sadat Golestan Hashemi[1,2], Manal Mosa Hosawi[1,2], Larissa Mourao[3], Paul Skipp[1,2,4], Xavier Morin[5], Colinda L.G.J. Scheele[3] and Salah Elias[1,2*]

[1]School of Biological Sciences, University of Southampton, Southampton, SO17 1BJ, United Kingdom

[2]Insitute for Life Sciences, University of Southampton, Southampton, SO17 1BJ, United Kingdom

[3]VIB-KULeuven Center for Cancer Biology, Herestraat 49, 3000, Leuven, Belgium

[4]Centre for Proteomic Research, University of Southampton, Southampton, SO17 1BJ, United Kingdom

[5]Ecole Normale Supérieure, CNRS, Inserm, Institut de Biologie de l'Ecole Normale Supérieure (IBENS), PSL Research University, Paris, France

*Correspondence: s.k.elias@soton.ac.uk

Abstract

Oriented cell divisions are critical for the formation and maintenance of structured epithelia. Proper mitotic spindle orientation relies on polarised anchoring of force generators to the cell cortex by the evolutionarily conserved $G_{\alpha i}$-LGN-NuMA complex. However, the polarity cues that control cortical patterning of this ternary complex remain largely unknown in mammalian epithelia. Here we identify the membrane-associated protein Annexin A1 (ANXA1) as a novel interactor of LGN in mammary epithelial cells. ANXA1 acts independently of $G_{\alpha i}$ to instruct the accumulation of LGN and NuMA at the lateral cortex to ensure cortical anchoring of Dynein-Dynactin and astral microtubules and thereby planar alignment of the mitotic spindle. Loss of ANXA1 randomises mitotic spindle orientation, which in turn disrupts epithelial architecture and lumen formation in three-dimensional (3D) primary mammary organoids. Our findings establish ANXA1 as an upstream cortical cue that regulates LGN to direct planar cell divisions during mammalian epithelial morphogenesis.

Introduction

Oriented cell divisions (OCDs) represent a fundamental mechanism for epithelial tissue morphogenesis, repair and differentiation during development and homeostasis [1]. Disruption in OCDs has direct implications for developmental disorders and cancer [1, 2]. OCDs are defined by the orientation of the mitotic spindle, which in turn determines the position and fate of daughter cells in epithelial tissue [1, 3]. Early studies have identified the evolutionarily conserved ternary complex formed by the $G_{\alpha i}$ subunit of heterotrimeric G proteins, the nuclear mitotic apparatus protein (NuMA) and LGN, as essential regulators that polarise force generators and capture astral microtubules at the cell cortex to orient the mitotic spindle [4]. During mitosis, LGN is recruited to the cell cortex through the interaction of its carboxy-terminal GoLoco motifs with GDP-bound $G_{\alpha i}$, which is anchored at the plasma membrane through myristoylation. The N-terminal tetratricopeptide repeat (TPR) domain of LGN interacts with NuMA that is released in the cytoplasm upon nuclear-envelope breakdown [4]. Polarized cortical localization of the $G_{\alpha i}$-LGN-NuMA complex is crucial for the interaction of NuMA with astral microtubules and recruitment of the Dynein-Dynactin motor complex through direct NuMA binding, which triggers minus-end directed movement of Dynein generating pulling forces on astral microtubules that position and orient the mitotic spindle [5]. $G_{\alpha i}$ subunits have a default distribution throughout the whole cell surface and do not contribute to the polarization of LGN at cortical crescents facing the spindle poles [6]. The mechanisms that polarize LGN at the cell cortex remain unfolding.

The orientation of the mitotic spindle in epithelia is instructed by polarity cues that translate external signals to pattern cortical LGN. The core members of the Par polarity complex (Par3, atypical protein kinase C (aPKC), and Par6), have been shown to play a key role in nearly every instance of OCDs [3, 4, 7]. In *Drosophila* neuroblasts, establishment of an apico-basal polarity axis allows the adapter protein Inscuteable (Insc) to accumulate at the apical cortex, where it binds to Par3 facilitating apical recruitment of LGN, to form a ternary complex that orients the mitotic spindle perpendicularly to the epithelial surface [8, 9]. Through the same mechanism, mammalian Insc (mInsc) controls perpendicular divisions in the mouse embryonic epidermis to promote stratification [10]. Combined loss of $G_{\alpha i}$ and mInsc in the murine epidermis

results in a shift towards planar divisions, suggesting that these occur by default in the absence of apical polarity cues [10]. Nonetheless, studies in canine kidney MDCK cells showed that phosphorylation of LGN by apical aPKC mediates its exclusion to the lateral cortex, favoring the planar orientation of the mitotic spindle [11]. Other polarity cues instruct lateral patterning of cortical LGN in mammalian epithelial. While, E-cadherin, Afadin, Disk large (Dlg), Ric-8A direct the recruitment of LGN at the lateral cortex [12-16], ABL1 and SAPCD2 act on its cortical accumulation and restriction [17, 18]. These diverse mechanisms that control LGN localization at restricted cortical domains have also been shown to act in a context-dependent manner.

The mammary gland is a unique organ that develops predominantly after birth and represents a powerful model system to study the mechanisms of adult mammalian epithelial morphogenesis. Postnatal morphogenesis of the mammary gland in response to hormonal stimuli drives dramatic tissue turnover and remodelling during successive pregnancies [19]. Despite the highly dynamic nature of the mammary epithelium, the contribution of OCDs to mammary epithelial morphogenesis remains ill-defined [3]. A few studies have shown that Aurora-A kinase (AurkA), Polo-like kinase 2 (Plk2), integrins, stathmin, huntingtin and Slit2/Robo1, control mitotic spindle orientation in mammary epithelial cells [20-25]. So far, only huntingtin and Slit2/Robo1 were reported to regulate cortical localization of LGN in the mammary epithelium [22, 25]. Recent evidence strongly suggests that OCDs affect cell fate outcomes in mammary stem/progenitor cells [3, 24, 26], and their dysregulation is linked to breast cancer development and aggressiveness [3, 24, 26, 27]. Thus, unravelling the molecular components and precise mechanisms of mitotic spindle orientation in the mammary epithelium remains an important priority.

Here we exploit affinity purification and mass spectrometry methods to characterize the cortical interactome of LGN in mitotic mammary epithelial cells. We identify Annexin A1 (ANXA1), a potent membrane-associated immunomodulatory protein and a biomarker that is differentially expressed in several types of breast cancer [28], as a novel LGN interactor that has not been reported previously to play any function in cell division. We demonstrate that ANXA1 interacts with LGN to restrict its distribution to the lateral cell cortex, thereby regulating the

dynamic and planar orientation of the mitotic spindle. ANXA1-mediated regulation of planar division is crucial for epithelial architecture and lumen formation in three-dimensional (3D) primary mammary organoids. Collectively the present experiments establish ANXA1 as a novel key polarity cue that instructs the accumulation of LGN at the lateral cell cortex, providing a mechanism that controls planar cell divisions during mammalian epithelial morphogenesis.

Results

LGN interactome in mitotic mammary epithelial cells

To identify LGN-binding proteins, we generated clonal MCF-10A mammary epithelial cells stably expressing GFP-LGN. GFP-expressing MCF-10A cells were used as controls. GFP-LGN display the same mitosis-dependent cortical localisation as compared to endogenous LGN (Supplementary Fig. 1a). The dynamics and duration of mitosis are not affected by the expression of GFP-LGN (Supplementary Fig. 1b). We used affinity purification to isolate the GFP-LGN complex from cells synchronised in mitosis (arrested in metaphase), and in interphase (arrested in G2 phase) (Supplementary Fig. 1c). We validated synchronisation efficiency by assessing the accumulation of phospho-Histone H3, and cellular distribution of LGN and microtubules (Supplementary Fig. 1d, e). Finally, we confirmed that the protocol specifically purifies the exogenous LGN in the GFP-LGN-bead-bound fractions as compared to controls (Supplementary Fig. 1f).

The purified GFP-LGN protein complex was trypsin-digested and analysed using liquid chromatography-tandem mass spectrometry (LC-MS/MS, see Methods for the technical details). All mass spectrometry proteomics data obtained from interphase and metaphase cells in two independent experiments have been deposited to the ProteomeXchange Consortium via the PRIDE partner repository [29]. Removal of proteins represented in the control beads, as well as common MS contaminants using the Contaminant Repository for Affinity Purification (CRAPome) database [30] and singletons identified an LGN/GPSM2 protein subnetwork of 18 proteins in metaphase cells (Fig. 1a, Supplementary Table 1). The LGN protein network includes known interactors such as NuMA, INSC and its partner PAR3 (Fig. 1a, Supplementary Table 1). Interestingly, our data suggest the NOTCH modulator NUMB, a regulator of asymmetric cell divisions [3], may form a complex with INSC and PAR3. A Gene Ontology (GO) analysis revealed that “spindle organization”, “establishment of spindle localization”, “regulation of spindle assembly”, “ciliary basal body-plasma membrane docking”, “spindle assembly”, “regulation of mitotic spindle organization”, “metaphase plate congression”, “regulation of protein localization to cell periphery”, “regulation of chromosome segregation”,

and “regulation of mitotic sister chromatid segregation”, are the most enriched biological process, and that the identified proteins were involved in pathways regulating mitosis progression, centrosome formation and maturation, microtubule organization (Fig. 1b, Supplementary Table 1). Several proteins involved in mitotic spindle assembly and orientation including PLK1, Dynein (DYNC1H1), p150^{Glued} (DCTN2), γ-tubulin (TUBG1), Cyclin B1 (CCNB1), RAN, CLASP1, HAUS6 and importin-α1 (KPNA2) [6, 31-46], were found in the LGN protein network by co-purifying with NuMA. We also identified the oncogene EIF3E (Eukaryotic translation initiation factor 3 subunit E)[46, 47], in the NuMA subcomplex. Finally, we identified a ternary complex comprising the membrane-associated protein Annexin A1 (ANXA1) [48] and its partner S100A11 (S100 Ca^{2+}-binding protein A11) [49], as well as the Serum Amyloid A-1 protein (SAA1) [50], that associates with LGN. We decided to gain more insight into this novel interaction. When we performed pull-down assays combined with western blotting analysis, we determined that GFP-LGN precipitates ANXA1 (Fig. 1c). Importantly, reciprocal immunoprecipitation shows that ANXA1-mCherry co-purifies with LGN (Fig. 1d). To further validate association between ANXA1 and LGN, we used an *in situ* proximity ligation assay (PLA). We detected proximity between ANXA1 and LGN in the cytoplasm and the cell cortex, where the signal was higher in metaphase as compared to interphase (Fig. 1e). Taken together these experiments uncover ANXA1 as a previously unknown interactor and potential regulator of LGN-mediated mitotic spindle orientation in mammalian epithelial cells.

Cell-cycle-dependent regulation of ANXA1 association with LGN at the cell cortex

Previous studies in post-mitotic epithelial cells established ANXA1 as a cytosolic protein that is recruited to the phospholipids of the plasma membrane and intracellular vesicular organelles, in a Ca^{2+}-dependent manner [51], but no mitosis-specific function has been reported for the protein. We characterised the cell-cycle dependent localization of ANXA1 in MCF-10A cells by immunofluorescence and confocal imaging. We observed that ANXA1 displays a consistent accumulation at the cell cortex, where it co-localises with LGN, NuMA and S100A11 during mitosis (Fig. 1f, Supplementary Fig. 2a), further indicating that ANXA1, LGN, NuMA and

S100A11 are part of the same macromolecular complex. Interestingly, a fraction of ANXA1 redistributes to the cytosol to localise around microtubules throughout mitosis (Supplementary Fig. 2b). We then further assessed the co-distribution of ANXA1 and LGN (Fig. 1f, Supplementary Fig. 2c). While LGN displays a diffuse cytosolic localisation in interphase, ANXA1 is uniformly distributed at the cell cortex (Fig. 1g, Supplementary Fig. 2c). At mitosis entry, LGN starts to relocate to the cell cortex where it colocalises with ANXA1. Consistent with previous studies [4], LGN is excluded from the central cortex during prometaphase, to polarise at the lateral cortex at metaphase. In sharp contrast, ANXA1 displays an opposite behaviour at the cell cortex during prometaphase whereby the protein accumulates centrally, while its amounts at the lateral cortex are lower as compared to LGN (Fig. 1f, g, Supplementary Fig. 2c). Moreover, before the metaphase plate finds a central position, ANXA1 and LGN display a mutually exclusive cortical-lateral distribution, with ANXA1 accumulating more at the closest lateral cortex to the chromosomes and LGN being more abundant at the opposing distant cortex (Fig. 1f). Once chromosomes are aligned centrally in metaphase, LGN distributes equally at the lateral cortex consistent with previous studies [6], while ANXA1 displays a more uniform, circumferential cortical distribution, a pattern observed until cytokinesis (Fig. 1f, g, Supplementary Fig. 2c). Collectively these experiments indicate that the distribution of ANXA1 along with LGN is spatiotemporally regulated and suggest ANXA1 as a potential regulator of LGN during mitosis.

ANXA1 restricts LGN localisation to the lateral cortex during mitosis

LGN orients the mitotic spindle by localizing NuMA and Dynein-Dynactin to the cell cortex [3, 4]. To investigate a possible function for ANXA1 in controlling LGN cortical localisation, we performed live imaging and assessed the effect of ANXA1 knockdown on the dynamic distribution of GFP-LGN in MCF-10A cells during mitosis. In cells transfected with a control siRNA (si-Control), we observed that GFP-LGN is recruited to the cell cortex during prometaphase to accumulate bilaterally at the cortex opposite to the spindle poles during metaphase (Fig. 2a, Supplementary Movie 1), consistent with previous studies in HeLa cells

[6]. The amounts of cortical GFP-LGN decrease progressively during anaphase, until telophase and cytokinesis where the protein redistributes to the cytosol (Fig. 2a). In contrast, siRNA-mediated knockdown of ANXA1 impairs significantly the dynamic distribution of GFP-LGN in ~78% of ANXA1-depleted cells (Fig. 2a-c). Close examination of these cells revealed cortical localisation of GFP-LGN is affected differentially upon ANXA1 knockdown (Fig. 2a, 2c, Supplementary Movie 2, Supplementary Movie 3, Supplementary Movie 4). We found that GFP-LGN remains at the central cortex in 50.37 ± 5.19% of ANXA1-depleted cells, while in 17.78 ± 3.40% the protein shows a circumferential distribution. Additionally, 10.37 ± 5.79% of ANXA1-depleted cells display a unilateral cortical accumulation of GFP-LGN. We did not find cells negative for cortical GFP-LGN in the absence of ANXA1, allowing us to conclude that ANXA1 acts on LGN restricted accumulation at the lateral cortex, rather than on its recruitment.

Next, we performed immunofluorescence and confocal imaging to evaluate the extent to which ANXA1 affects the ability of LGN to localise NuMA and the p150^{Glued} Dynactin subunit to the lateral cortex during metaphase. In agreement with our live imaging results, siRNA-mediated knockdown of ANXA1 prevents the bilateral cortical accumulation of LGN, with the protein displaying central (si-ANXA1#1: 53.33 ± 7.70%; si-ANXA1#2: 43.02 ± 8.76%), circumferential (si-ANXA1#1: 19.68 ± 3.86%; si-ANXA1#2: 25.7 ± 1.50 %), or unilateral (si-ANXA1#1: 16.51 ± 5.20%; si-ANXA1#2: 14.26 ± 7.20%) distributions in ANXA1-depleted cells (Fig. 2d, e). Similarly, ANXA1 knockdown impairs NuMA cortical-lateral restriction, which displays a central distribution in a large proportion of ANXA1-depleted cells (si-ANXA1#1: 35.71± 7.14%; si-ANXA1#2: 27.34± 8.77%) (Fig. 2d, e). By contrast, we found p150^{Glued} was absent at the cell cortex in the majority (si-ANXA1#1: 48.60 ± 3.01%; si-ANXA1#2: 48.46 ± 0.79%) of ANXA1-depleted cells (Fig. 2d, e), indicating an impairment in its cortical recruitment. Interestingly, ANXA1 knockdown did not affect $G_{\alpha i}$ cortical distribution (Fig. 2f, g). Thus, ANXA1 is required to localise the LGN-NuMA-Dynein-Dynactin complex at the lateral cortex during mitosis, independently of $G_{\alpha i}$.

ANXA1 acts upstream of LGN to regulate mitotic progression and spindle orientation

Proper cortical localisation of the LGN-NuMA-Dynein-Dynactin complex is required to generate polarised pulling forces on astral microtubules that orient the mitotic spindle [4]. The results above strongly suggest that ANXA1 regulates mitotic spindle positioning. To test this possibility, we performed live imaging in control and ANXA1-depleted MCF-10A cells, in which we labelled microtubules with SiR-tubulin [52] and DNA with Hoechst 33342. First, we observed significant defects in the dynamics of cell division in a vast majority of ANXA1-depleted cells (90.95 ± 2.15%) as compared to controls (12.04 ± 2.45%) (Fig. 3a, b, Supplementary Movie 5, Supplementary Movie 6, Supplementary Movie 7, Supplementary Movie 8). The proportion of cells that completed mitosis decreases significantly upon ANXA1 knockdown (si-ANXA1#1: 57.14 ± 9.18%, versus si-Control: 100± 0.00%) (Fig. 3c). In ANXA1-depleted cells that completed mitosis, the duration of the mitotic process is significantly extended as revealed by increased transition time from nuclear envelop breakdown (NEBD) to anaphase onset (si-ANXA1#1: 54.11 ± 1.08 min versus si-Control: 38.56 ± 1.52 min) (Fig. 3d). The size and morphology of the mitotic spindle are affected as well, with ~36% and ~14% of ANXA1-depleted cells displaying abnormal bipolar or multipolar spindles, respectively (Fig. 3e). Our analyses also reveal that ANXA1 knockdown results in chromosome segregation defects in ~36% of cells (Fig. 3e). During metaphase, ~82% of ANXA1-depleted cells display excessive oscillations of the mitotic spindle relative to the z axis between successive time frames, whereas in control cells the spindle does not display notable oscillatory z rotations and remains in a planar position (Fig. 3f-h). We further confirmed these observations using immunofluorescence and confocal imaging, which show virtually all mitotic spindles in the controls orient parallel to the substratum plane (3.87° ± 0.37°), whereas ANXA1-depleted cells display spindle orientation defects (si-ANXA1#1: 15.45° ± 0.77°; si-ANXA1#2: 18.53° ± 2.02°) (Supplementary Fig. 3a, b). Live imaging experiments also show a significant increase in mitotic spindle oscillatory rotations within the xy plane upon ANXA1 knockdown, with spindle oscillation frequencies significantly higher as compared to controls (Fig. 3i-k). Remarkably,

whereas in control cells mitotic spindles mostly oscillate around their initial position at metaphase onset, ANXA1-depleted cells display random spindle displacements (Fig. 3l), where average movements away from the original position are significantly higher as compared to control (si-ANXA#1: 2.56 ± 0.09 μm versus si-Control: 1.80 ± 0.17 μm) (Fig. 3m). Spindle displacement speed was not affected upon ANXA1 depletion (si-ANXA#1: 0.32 ± 0.05 μm/min versus si-Control: 0.27 ± 0.02 μm/min) (Fig. 3n). Together, these data indicate that ANXA1 is required for proper mitotic spindle positioning and assembly, faithful chromosome segregation to daughter cells, as well as mitotic progression.

We next tested whether ANXA1 lies upstream of LGN, using immunofluorescence and confocal imaging. Consistent with previous studies [15, 53-55], we found that siRNA mediated LGN knockdown results in mitotic spindle misorientation, with spindle angles αz increasing from 3.14° in controls to 13.80° and 17.21° in cells treated with si-LGN#1 and si-LGN#2, respectively (Supplementary Fig. 3c, d). However, LGN depletion does not affect the cortical distribution of ANXA1, whereas it impairs the recruitment of NuMA to the lateral cortex (Supplementary Fig. 3e, f). These data allow us to conclude that ANXA1 acts upstream of LGN to control mitotic spindle orientation.

The anchoring of astral microtubules to the cell cortex, and the regulation of their number and stability by the LGN-NuMA-Dynein-Dynactin complex are key to ensure correct mitotic spindle orientation and assembly [4]. We therefore examined microtubule stability and dynamics upon ANXA1 knockdown in mitotic cells. Using immunofluorescence and confocal imaging, we show that ANXA1 knockdown results in elongation and buckling of astral microtubules, while their overall intensity and number remain not significantly affected, suggesting their higher stability (Supplementary Fig. 4a-c). Astral microtubule elongation and stabilization correlate with spindle misplacement close to one side of ANXA1-depleted cells, suggesting imbalance in the forces exerted on the mitotic spindle (Supplementary Fig. 4d). These results are in line with our earlier observations showing an increase in mitosis duration and proportion of cells displaying abnormal mitotic spindles in ANXA1-depelted cells. Thus, ANXA1 is required for

proper microtubule-cortex crosstalk to ensure accurate spindle assembly and mitotic progression.

ANXA1 is expressed in luminal cells and required for planar cell divisions and epithelial morphogenesis

Differential expression of ANXA1 affects mammary epithelial integrity promoting tumour initiation, epithelial-to-mesenchymal transition (EMT) and metastasis [28]. However, how ANXA1 regulates normal mammary epithelial homeostasis and morphogenesis remains unknown. To characterize ANXA1-expressing cells *in vivo*, we performed immunostaining experiments in mouse adult virgin mammary glands. We reveal that ANXA1 expression is restricted to the luminal epithelial compartment, where ANXA1^{+} cells selectively co-express the luminal marker E-cadherin and not the basal marker keratin (K)14 (Fig. 4a). Consistent with our observations in MCF-A10 cells, ANXA1 is mostly detected at the cell cortex of luminal cells (Fig. 4a). Thus, we conclude that ANXA1 is a specific luminal surface marker in the mammary epithelium.

Next, we tested the effect of ANXA1-mediated regulation of mitotic spindle orientation on the ability of primary luminal mammary epithelial cells (MECs) to form organoids in 3D culture. We isolated MECs from mouse mammary glands at days 15.5-16.5 of pregnancy (P15.5-P16.5) and cultured them within Matrigel [56]. Using immunofluorescence and confocal imaging we first characterised MECs division modes throughout epithelial morphogenesis, as this has not been described previously (Fig. 4b-d). At 48 hours (48h) of culture, ~64% of MECs align their mitotic spindle planar to the basement membrane (angle α 0°-30°), whereas the proportion of MECs displaying planar divisions increases to ~90 and ~89 at 72h and 96h, respectively (Fig. 4b, c). This increase in planar divisions is accompanied with a re-organization of MECs around an expanding single central lumen that matures at 120h, where MECs cease to divide and complete their apico-basal polarisation, as revealed by the accumulation of F-actin at their apical surface (Fig. 4b). Consistent with our results in MCF-10A cells, ANXA1 distributes at the cell cortex during mitosis in MECs (Fig. 4d). To investigate the effect of ANXA1 knockdown on mitotic spindle orientation in 3D culture, we generated

MECs expressing control or ANXA1 short hairpin (sh) RNAs (sh-Control versus sh-ANXA1#1 or sh-ANXA1#2) (Fig. 4e). As expected, ~87% of control MECs display planar cell divisions in 72h organoids (Fig. 4f, g). In sharp contrast, ANXA1-depleted MECs fail to align planar mitotic spindles, with ~69% and ~70% of mitotic cells dividing perpendicularly to the epithelial plane with spindle angles α greater than 30°, upon sh-ANA1#1 or sh-ANXA1#2 treatment, respectively (Fig. 4f, g). Moreover, while LGN localises at the lateral cortex in control mitotic MECs, ANXA1 depletion impairs its polarised cortical distribution (Fig. 4h). Together, these data indicate that ANXA1 is required for MECs planar cell divisions during morphogenesis.

By 120h of 3D culture, control organoids are mono-layered with a single central lumen, whereas ANXA1-depleted MECs form larger, disorganised, and multi-layered organoids, with multiple small or collapsed lumen (Fig. 4i-k). While controls are circular, ANXA1-depleted organoids display irregular and elongated shapes, further indicating aberrant epithelial architecture (Fig. 4i, j). Our experiments suggest that mitotic spindle misorientation upon ANXA1 knockdown results in daughter cells generated perpendicularly to the epithelial plane, thereby leading to epithelial cell multi-layering and lumen filling. Interestingly, this mechanism leading to the escape of cells out of the epithelial sheet has been proposed to impair epithelial architecture and contribute to tumour initiation [57]. Consistent with this, ANXA1-depleted MECs display dramatic cytoarchitectural defects and fail to acquire correct apico-basal polarity as revealed by misslocalised E-cadherin and F-actin (Fig. 4i, l). Thus, ANXA1-mediated regulation of planar mitotic spindle orientation ensures normal epithelial morphogenesis.

Discussion

Oriented cell divisions (OCDs) are essential for establishing proper epithelial tissue architecture and function [3, 4]. Our molecular knowledge of the mechanisms that align the mitotic spindle in polarised epithelia has advanced, in large part from extensive studies in model systems in the genetically tractable *Drosophila melanogaster* and *Caenorhabditis elegans* [3, 4]. The $G_{\alpha i}$-LGN-NuMA ternary complex is established as an evolutionarily conserved spindle orientation machinery that anchors the Dynein-Dynactin force generator complex and astral microtubules to the cell cortex, ensuring correct cell division orientation to achieve proper tissue morphogenesis and differentiation [3, 4]. However, the molecular mechanisms governing mitotic spindle positioning in mammalian epithelia remain poorly defined. The present experiments uncover ANXA1, a membrane-associated protein, as a novel interactor of LGN, regulating planar mitotic spindle orientation for correct mammary epithelial morphogenesis. We further report that ANXA1 is an upstream cortical cue that instructs LGN and NuMA polarised accumulation at the lateral cortex, ensuring balanced Dynein-Dynactin-mediated pulling forces on astral microtubules and correct alignment of the mitotic spindle (Fig. 5).

Our findings demonstrate that ANXA1 regulates LGN restricted distribution to the lateral cortex instead of its $G_{\alpha i}$-mediated recruitment. We propose that ANXA1 controls LGN cortical localization by mediating its exclusion from the central cortex during prometaphase and ensuring its stable accumulation at the lateral cortex at metaphase. In line with this, we show that ANXA1 depletion results in a central and circumferential cortical distribution of LGN and its partner NuMA. Similar regulatory mechanisms mediated by PLK1, the cortical polarity proteins ABL1 and SAPCD2, as well as the chromosome derived RanGTP gradient, have been shown to restrict the localisation of LGN at the cortex to maintain the spindle orientation axis [6, 17, 18, 58]. It will be key to dissect the mechanisms underlying the assembly and spatiotemporal dynamics of the ANXA1-LGN complex at the cortex and understand how this synergizes with $G_{\alpha i}$-mediated recruitment of LGN.

We show that disruption of the polarized cortical localisation of the LGN-NuMA-Dynein-Dynactin complex upon ANXA1 depletion leads to elongated and buckled astral microtubules

affecting the assembly and orientation of the mitotic spindle, pointing out to a critical role of ANXA1 in the regulation of cortical pulling forces on astral microtubules that control the dynamics of the mitotic spindle. Our live imaging experiments also reveal that ANXA1 depletion leads to incorrect chromosome segregation and delay in mitotic progression. Mitotic spindle orientation defects can be caused by incorrect metaphase plate formation and chromosome misalignment [58]. This raises the question of whether the errors that we observe in chromosome segregation are independent of defects in mitotic spindle orientation in ANXA1-depeleted cells. Nonetheless, our cortical LGN interactome data identify several NuMA-interacting proteins that have been described to play multiple roles in the regulation of astral microtubule stability, mitotic spindle positioning, and kinetochore-microtubule dynamics, including the DYNC1H1/Dynein-p150^{Glued}/Dynactin complex [6, 32-36, 59], CLASP1 [37-39], HAUS6 [40, 41], KPNA2/Importin-α [60], PLK1 [6, 31], TUBG1/γ-tubulin [41, 42], EIF3E/Int-6 [47], CCNB/CDK1 [36, 43], RAN [39, 44, 45]. Thus, our findings indicate that defects in astral microtubules and spindle orientation upon ANXA1 depletion are likely to cause incorrect chromosome segregation. This is consistent with evidence suggesting that unbalanced astral microtubule-cortex cross talk leads to defective chromosome dynamics [4, 61]. It will be interesting to explore further the molecular mechanisms linking ANXA1-mediated regulation of astral microtubule dynamics to accurate chromosome segregation.

It is possible that ANXA1 maintains the balanced forces on astral microtubules by regulating microtubule-actin crosstalk at the cell cortex, a key mechanism that defines the mitotic spindle orientation axis [62]. In fact, the protein has been shown to bind and bundle F-actin in a Ca^{2+}-dependent manner [63]. Recent studies have shown that ANXA1 Ca^{2+}-dependent translocation to the inner leaflet of the plasma membrane facilitates its interaction with its partner S100A11 at lamellipodial extrusions of migrating cells to regulate membrane and F-actin dynamics [64, 65]. Furthermore, ANXA1 was also suggested to influence actin dynamics via a direct interaction with the actin polymerising profiling [66, 67]. While the mechanisms remain unknown, this interaction was shown to regulate both the ability of ANXA1 to bind phospholipids and the effects of profilin on actin polymerization. Additionally, ANXA1 interacts with vimentin, a key F-

actin-binding protein that regulates cortical actin organisation and mechanics, which allows normal mitotic progression [68-70]. Finally, our observations showing that a fraction of cytosolic ANXA1 localises to microtubules and the mitotic spindle suggest that ANXA1 may also directly modulate microtubule dynamics. Uncovering the molecular mechanisms allowing ANXA1 to regulate actin and microtubule dynamics and their crosstalk at the cell cortex will provide important novel insights into the role that ANXA1 plays in the regulation of the pulling forces that orient the mitotic spindle to its correct position.

Regulation of the LGN-NuMA-Dynein-Dynactin complex is essential to maintain the balance between planar and perpendicular divisions that ensures proper position and fate of daughter cells during epithelial morphogenesis and differentiation [3, 4]. Our data in organoids of primary luminal MECs demonstrate that ANXA1-mediated regulation of LGN cortico-lateral localisation and planar spindle orientation is pivotal for normal lumen formation and epithelial architecture. This is consistent with studies in MDCK, Caco-2 and hepatocytic HepG2 cells establishing LGN as a key regulator of planar cell division during cystogenesis [11, 13, 55, 71, 72]. In MDCK cells, maturation of the apical membrane is required for aPKC-dependent exclusion of LGN to the lateral cortex, ensuring planar cell division and lumen formation [11]. Our experiments in MEC organoids suggest, however, that LGN lateral accumulation does not need mature apical polarity, further sustaining our model establishing ANXA1 as an essential polarity cue that instructs LGN restriction to the lateral cortex. Moreover, our data showing that apical polarity is established at d5 of 3D culture after cells have ceased to divide strongly suggest that lumen formation and expansion is driven by planar cell divisions, independently of apical polarity. Interestingly, our proteomic data also identify another LGN-interacting ternary complex including the LGN adapter INSC and the polarity proteins PAR3 and NUMB. While these proteins have been widely established as essential regulators of apical localization of LGN and asymmetric/perpendicular cell division [3, 4], a study in the mouse mammary gland has shown that overexpression of INSC leads to a shift in the mode of division of stem cells from asymmetric/perpendicular to symmetric/planar [25], indicating a role of INSC in the regulation of planar cell division in the mammary epithelium. These findings also point out to the context-

dependent action of the regulatory mechanisms that control the localization and function of the LGN-NuMA-Dynein-Dynactin complex. How ANXA1 acts with INSC-PAR3-NUMB to regulate the LGN-mediated planar mitotic spindle orientation remains to be determined.

The balance between symmetric and asymmetric division is broken in breast cancer [3, 24, 26, 27, 73]. Yet, it remains unknown how incorrect mitotic spindle orientation can initiate breast tumorigenesis. Studies in the normal prostate epithelium have shown that depletion of E-cadherin affects the localisation of the LGN-NuMA complex and randomises mitotic spindle orientation, resulting in prostatic hyperplasia that progress to invasive adenocarcinoma [14]. Thus, defects in OCDs can be envisioned as a key initiating oncogenic event. Our 3D culture experiments show that depletion of ANXA1 leads to epithelial multi-layering, resulting in aberrant epithelial architecture and multiple off-centred small or collapsed lumens, reminiscent of the cribriform growth pattern that is often observed in breast ductal carcinoma *in situ* (DCIS) [74]. Indeed, cell division-driven epithelial multi-layering where cells escape from the epithelial sheet has been proposed to represent one of the early steps in tumorigenesis [57]. ANXA1 is well established as a biomarker of breast cancer [28]. While the underlying mechanisms remain poorly understood, studies have shown that ANXA1 is downregulated in DCIS whereas it is upregulated in the most aggressive and metastatic breast cancer subtypes [28]. Interestingly, here we show that ANXA1 specifically marks a subset of luminal epithelial cells in the mouse mammary gland *in vivo*. It will be particularly interesting to investigate the functional requirement of ANXA1-mediated mitotic spindle orientation for proper mammary epithelial integrity and differentiation *in vivo*. In parallel, it will also be highly informative to learn more about the fate and dynamics of ANXA1-expressing cells and their relative contributions to mammary gland development and homeostasis, but also to tumour formation and heterogeneity.

Methods

Cell lines and transfections

MCF-10A, a spontaneously immortalized, nontransformed human mammary epithelial cell line (ATCC®) was cultured in DMEM/F12 (Invitrogen) supplemented with 5% donor horse serum (Gibco), 20 ng/ml EGF (PeproTech), 10 µg/ml insulin (Sigma), 1 ng/ml cholera toxin (Sigma), 100 µg/ml hydrocortisone (Sigma), 50 U/ml penicillin, and 50 µg/ml streptomycin (Life Technologies), at 37°C in a humidified 5% CO_2 atmosphere. Cells were transfected with a final concentration of 50 nM si-RNAs using Lipofectamine RNAiMAX (Invitrogen), according to the manufacturer's protocol. Cells were lysed or fixed and immunoprocessed 72h after transfection.

HEK293 cells provided by Melissa Andrews (University of Southampton), were cultured in DMEM supplemented with 10% FBS (Gibco), 50 U/ml penicillin, and 50 µg/ml streptomycin (Life Technologies), at 37°C in a humidified 5% CO_2 atmosphere. Cells were transfected using standard calcium phosphate transfection protocol [75].

Primary mammary epithelial cell 3D culture

Primary mammary epithelial cells (MECs) were collected from wild-type C57Bl/6 15.5- and 16.5-day pregnant mice and cultured as described [56]. Cells (2×10^4) were plated in each well of 8-well LabTekII chamber slides (Fisher Scientific) pre-coated with Phenol-free Growth Factor Reduced 100% Matrigel (25 µl per well, BD Biosciences) and cultured in DMEM-F12 supplemented with 2% Matrigel, 10% FBS (Gibco), 3 ng/ml EGF (PeproTech), 1% Glutamine (Sigma), 1 µg/ml Hydrocortisone (Sigma), 10 µg/ml Insulin (Sigma) and 1% Penicillin/Streptomycin (Life Technologies). Cells were grown onto Matrigel to form organoids for 2-5 days and fed every 2 days. All animal experiments were performed in accordance with Home Office (UK) regulations and approved by the University of Southampton Local Ethical Committee.

Constructs, siRNAs and shRNAs

Retroviral plasmids were used to transduce MCF-10A cells. pTK14-GFP-LGN plasmid was obtained from Addgene (Plasmid #37360). pTK-GFP was cloned as follows: The full-length eGFP sequence from pTK14 plasmid was amplified by PCR and inserted into the pTK14 plasmid, where the GFP-LGN sequence was removed by restriction digestion with Bsu36i and PspOMI (New England Biolabs). The primers were 5'-CCGACCTGAGGAAGGGAG3-3' (forward) and 5'-ACAGCGGGGCCCTTACTTGTACAGCTCGTCCATGCC-3' (reverse). To clone pTK-ANXA1-mCherry, the ANXA1-mCherry sequence was synthesised (Eurofins) and inserted into pTK93-Lifeact-mCherry vector (Addgene, Plasmid #46357) where Lifeact-mCherry was removed by restriction digestion with NaeI and ApaI (New England Biolabs). pTK-mCherry was cloned as follows: The full-length mCherry sequence was amplified by PCR and inserted into pTK93-Lifeact-mCherry vector where the Lifeact-mCherry sequence was removed by restriction digestion with BamHI and SalI (New England Biolabs). The primers were 5'-AATTGGATCCGCCACCATGGTGAGCAAGGGCGAG-3' (forward) and 5'-CTGACACACATTCCACAGGGTCG-3' (reverse). For all plasmids, correct insertions were verified by Sanger sequencing.

Transient knockdown of human ANXA1 or LGN in MCF-10A cells was achieved by transfection of MISSION® Predesigned siRNAs from Sigma. The following products were used: SASI_Hs01_00157996 (si-ANXA1#1), SASI_Hs01_00157997 (si-ANXA1#2) for ANXA1 knockdown; SASI_HS01_00121831 (si-LGN#1), SASI_HS01_00121832 (si-LGN#2) for LGN knockdown. siGENOME RISC-Free® (Dharmacon) was used as a negative control (si-Control).

Stable knockdown of mouse ANXA1 in MECs was performed by small-hairpin RNAs (sh-RNAs). shRNA sequences were annealed and cloned into the pLKO.4-Mem-Venus lentiviral vector, provided by David Bryant (CRUK Beatson Institute University of Glasgow). The following sh-RNA sequences were used: 5'-CCGGGCTTTGGCAGATAAGTCTAATCTCGAGATTAGACTTATCTGCCAAAGCTTTTTG-3' (sh-ANXA1#1 forward) and 5'-CCGGCCGTTCGGAAATTGACATGAACTCGAGTTCATGTCAATTTCCGAACGGTTTTTG-3'

(sh-ANXA1#1 reverse); 5'-AATTCAAAAAGCTTTGGCAGATAAGTCTAATCTCGAGATTAGACTTATCTGCCAAAGC-3' (sh-ANXA1#2 forward) and 5'-AATTCAAAAACCGTTCGGAAATTGACATGAACTCGAGTTCATGTCAATTTCCGAACGG-3' (sh-ANXA1#2 reverse). As a negative control, the following sequences were used: 5'-CCGGCCTAAGGTTAAGTCGCCCTCGCTCGAGCGAGGGCGACTTAACCTTAGGTTTTTG-3' (sh-Control forward) and 5'-AATTCAAAAACCTAAGGTTAAGTCGCCCTCGCTCGAGCGAGGGCGACTTAACCTTAGG-3' (sh-Control reverse).

Lentivirus and retrovirus production and infection

To generate stable MCF-10A cell lines, plasmids were introduced by retroviral transduction. Retroviruses were prepared in HEK293 cells by calcium phosphate co-transfection of 10 µg retroviral plasmid, 6.5 µg envelope plasmid pCMV-VSV-G (Addgene, Plasmid #8454) and 5 µg packaging plasmid pUMVC (Addgene, Plasmid #8449). Virus particles were collected 48 h after transfection, filtered (45 µm) and used to infect MCF-10A cells in the presence of 8 µg/ml polybrene (Sigma-Aldrich). Clones of interest were selected using 2 µg/ml blasticidin (Sigma) or 1 µg/ml puromycin (Sigma). To further enrich for positive cells, selected cells were subjected to flow-cytometry to sort for fluorescent-positive cells.

Knockdown of ANXA1 in MECs was achieved by lentiviral transduction. Lentiviruses were generated similarly to retrovirus production by co-transfecting 10 µg lentiviral plasmid, 10 µg envelope plasmid pCMV-VSV-G and 10 µg packaging plasmid (pPAX2). pPAX2 plasmid was provided by David Bryant (CRUK Beatson Institute, University of Glasgow). Freshly isolated MECs were transduced as described [76], and cultured in 8-well slide chambers pre-coated with Matrigel to form organoids until immunoprocessing.

Cell cycle synchronization

Drugs were dissolved in DMSO and kept at -20°C as 10 mM stock solutions. To synchronize MCF-10A cells in G2/M phase, cells were treated with 9 µM RO-3306 (Calbiochem) for 18h to allow CDK1 inhibition. To further arrest cells in metaphase, MCF-10A cells were released from the G2/M block by washing three times with prewarmed drug-free media and immediately treated with 10 µM proteasome inhibitor MG-132 (Calbiochem) for 6h. Cells were washed twice with PBS before processing for experiments.

Cell extracts and immunoblotting

MCF-10A cells and MEC 3D organoids were lysed in NP-40 buffer [50 mM Tris, pH 7.4, 250 mM NaCl, 5 mM EDTA, 50 mM NaF, 1 mM Na3VO4, 1% Nonidet P40 (NP40)], supplemented with protease inhibitor cocktail (Sigma, #P2714). MEC organoids were first treated with trypsin 0.25% for 30 min to break the Matrigel, then washed with PBS1X and resuspended in NP40 lysis buffer, containing protease inhibitor cocktail, and centrifuged at 14,800 x rpm for 10 min at 4°C. Protein concentration of lysates was determined using Pierce™ BCA Protein Assay (ThermoScientifc) and protein were subjected to SDS-PAGE and subsequent Western blot analysis. The following primary antibodies were used: anti-α-tubulin DM1A (1:5000, Sigma #T6199), anti-LGN (1:500, Sigma #ABT174), anti-GFP (1:1000, Invitrogen #A-11122), anti-phospho-Histone3 (1:1000, Sigma #06-570), anti-ANXA1 (1:500, Proteintech, #55018-1-AP), anti-mCherry (1:1000, Abcam #ab167453). Secondary antibodies conjugated to horseradish peroxidase (Invitrogen, #32430, #32460) were used at 1:10,000. Protein bands were visualized using SuperSignal™ West Femto Substrate (Thermo Scientific) on a Syngene PXi detection system (Syngene).

Immunoprecipitation and sample preparation for mass spectrometry

MCF-10A cells were plated in 15 cm dishes and washed twice with ice-cold PBS before protein extraction. About 10 x 10^7 cells were lysed in a mild lysis buffer [50 mM Tris, pH 7.4, 150 mM NaCl, 0.5 mM EDTA, 10 mM NaF, 1 mM Na3VO4, 0.5% Nonidet P40 (NP40)], containing

protease inhibitor cocktail. Cell lysates were cleared by centrifugation at 17,000x g for 30 min at 4°C. Co-immunoprecipitation was performed using a GFP- or RFP-Trap Kit (Chromotek, #gtma-20, #rtma-20) as per manufacturer's instructions. For immunoblotting, washed beads were eluted by boiling in Laemmli sample buffer (Bio-Rad) containing 5% 2-mercaptoethanol. For mass spectrometry analysis, washed beads were eluted by on-bead tryptic digestion as described [77, 78]. Briefly, proteins on the beads were partially denatured with a buffer containing 2 M urea in 50 mM Tris, pH 7.5, 1 mM DTT. Beads were further treated with a buffer containing 2 M urea in 50 mM Tris, pH 7.5, 5 mM iodoacetamide (IAA) and proteins were eluted by digestion with 5 µg/ml trypsin (Promega). Eluted proteins were fully digested overnight. C18 reverse phase clean-up was performed on the tryptic peptides using a Waters Oasis C18 plate (Waters, UK).

Mass spectrometry and data analysis

Peptide extracts were separated on an Ultimate 3000 RSLC nano system (Thermo Scientific) using a PepMap C18 EASY-Spray LC column, 2 µm particle size, 75 µm x 75 cm column (Thermo Scientific) over a 140 min (single run) linear gradient of 3–25% buffer B (0.1% formic acid in acetonitrile (v/v)) in buffer A (0.1% formic acid in water (v/v)) at a flow rate of 300 nL/min. Peptides were introduced using an EASY-Spray source at 2000 V to a Fusion Tribrid Orbitrap mass spectrometer (Thermo Scientific). Full MS spectra were recorded from 300 to 1500 *m/z* in the Orbitrap at 120,000 resolution with an automatic was performed using TopSpeed mode at a cycle time of 3 s. Higher-energy collisional dissociation (HCD) fragmentation was induced at an energy setting of 28 for peptides with a charge state of 2–4. Fragments were analyzed in the orbitrap at 30,000 resolution. Analysis of raw data was performed using Proteome Discoverer software (Thermo Scientific) and the data processed to generate reduced charge state and deisotoped precursor and associated product ion peak lists. These peak lists were searched against the human Uniprot KB database protein database (42,186 entries, 2018-05-18). A maximum of one missed cleavage was allowed for tryptic digestion and the variable modification was set to contain oxidation of methionine and N-terminal protein acetylation.

Carboxyamidomethylation of cysteine was set as a fixed modification. The false discovery rate (FDR) was estimated with randomized decoy database searches and were filtered to 1% FDR. Proteins present in the control were removed and further contaminants were also removed by searching against the Contaminant Repository of Affinity Purification (CRAPome) database [30]. The interactions network was constructed with the online STRING protein-protein interaction (PPI) database (v. 11) [79] using an interaction confidence score of ≥ 0.6. The PPI networks were visualized and analysed using Cytoscape software (version 3.8.2) [80]. Gene enrichment analyses were performed to identify Gene Ontology (GO) biological process as well as Reactome and KEGG (Kyoto Encyclopedia of Genes and Genomes) pathways associated with the PPI networks using ClueGO plugin of Cytoscape (version 2.5.7) [81].

Immunofluorescence

The following primary antibodies were used: anti-LGN (1:200, Sigma #ABT174), anti-NuMA (1:100, Novus Biologicals #NB500-174), anti-p150^{Glued} (1:100, BD Biosciences #610473), anti-γ-tubulin AK-15 (1:300, Sigma #T3320), anti-$G_{\alpha i}1$ (1:20, Santa Cruz #sc-56536), anti-ANXA1 (1:100, Proteintech #66344-1-Ig, #21990-1-AP), anti-S100A11 (1:100, Proteintech #60024-1-Ig), anti-α-tubulin DM1A (1:1000, Sigma #T6199), anti-E-cadherin (1:100, Invitrogen #13-1900), anti-keratin 14 (K14) (1:500, Biolegend #PRB-155P) and anti-GFP (1:300, Sigma #11814460001). AlexaFluor 555 phalloidin (1:200, Life Technologies #A34055) was used to label F-actin. Secondary antibodies (Life Technologies) used were goat anti-mouse (#A32723), anti-rabbit (#A11037 and #A11008), anti-rat (#A11007) and anti-guineapig (#A21450) conjugated to AlexaFluor-488, AlexaFluor594 or AlexaFluor-647, at 1:400 dilutions.

To visualise LGN, NuMA, P150^{Glued}, ANXA1, GFP and γ-tubulin, MCF-10A cells were fixed with anhydrous methanol at -20°C for 10 min followed by permeabilization with 0.1% Triton X-100 in PBS for 2 min. Alternatively, cells were fixed with 10% trichloroacetic acid (TCA) for 7 min on ice followed with anhydrous methanol at -20°C for 10 min. Cells were washed three times before permeabilization with 0.1% Triton X-100 in PBS for 2 min. $G_{\alpha i1}$ and α-tubulin were visualized by fixing cells with 4% paraformaldehyde (PFA) for 20 min at RT followed by

permeabilization with 0.5% Triton X-100-PBS for 10 min. For all fixation methods, cells were blocked with 3% BSA in 0.1% Triton X-100 in PBS for 1h at RT and immunostained with primary antibodies overnight at 4°C. Cells were washed and incubated with appropriate secondary antibodies for 1h at RT.

To visualize astral microtubules, MCF-10A cells were fixed with 3 % PFA, containing 0.25% glutaraldehyde and 0.2% NP-40 in Brinkley buffer 1980 [(BRB80) 80 mM PIPES, 1 mM MgCl2 hexahydrate, 1 mM EGTA] for 1 min, followed by incubation with 3% PFA and 0.25% glutaraldehyde in BRB80 for 10 min and with 0.1 M NH_4Cl in BRB80 for 10 min. Cells were washed twice for 5 min with BRB80, permeabilized with 0.5% Triton X-100 in PBS for 10 min, washed again twice in BRB80 and finally blocked in 3% BSA and 0.2% NP-40 in BRB80 for 1h.

For all MCF-10A cell immunostaining, cells were counterstained with 2.5 µg/ml Hoechst 33342 (Sigma) and mounted with Vectashield mounting medium (Vector Laboratories).

MEC organoids were fixed with 4% PFA for 30 min and permeabilized with 0.5% Triton X-100 in PBS for 10 min. Organoids were blocked with 1 % BSA in PBS and 0.1% Triton X-100 for 2h and then incubated with ANXA1, LGN, α-tubulin, E-cadherin primary antibodies overnight at 4°C. Then, organoids were immunostained with mouse, rabbit, and rat AlexaFluor488-, AlexaFluor594- or AlexaFluor647-conjugated secondary antibodies for 2h at RT. Organoids with F-actin staining at the apical surface of cells surrounding a single lumen were identified as organoids with normal lumens. Cells were counterstained with DAPI-containing Fluoroshield (Sigma).

Mammary gland sections (50 µm thick) were cut and air-dried for 30 min, then fixed with 4% PFA for 20 min at RT. Following 45 min permeabilization with 0.2% Triton X-100 in PBS, slides were blocked for 2 h in 2% BSA, 5% foetal bovine serum (FBS), 0.2% Triton X-100 in PBS. Sections were incubated at 4°C overnight in ANXA1, E-cadherin and K14 primary antibodies, washed and incubated with rabbit, rat and guineapig AlexaFluor488-, AlexaFluor594- and AlexaFluor647-conjugated secondary antibodies for 2h at RT. Sections were counterstained with DAPI-containing Fluoroshield.

Proximity ligation assay

To detect proximal association of ANXA1 and LGN, the Duolink™ proximity ligation assay (PLA) (Sigma, #DUO92102) was used according to the manufacturer's protocol. Briefly, MCF-10A cells expressing GFP-LGN were fixed and stained as described in the standard immunofluorescence protocol above. Samples were incubated with AXNA1 and GFP primary antibodies overnight at 4°C. As a negative control, cells were incubated with ANXA1 antibody alone. Cells were incubated with Duolink PLA probes for 2h, washed and incubated with the ligation mixture for 30 min, washed again and incubated with the amplification mixture for 2.5h. Cells were counterstained with DAPI-containing Fluoroshield.

Quantitative confocal microscopy

Immunofluorescence images were captured with an inverted Leica TCS SP8 inverted laser scanning microscope (Leica Microsystems) using x40 oil immersion (40x HC Plan/Apo CS2 1.30 numerical aperture (NA)) and x63 glycerol immersion (63x HC Plan/Apo CS2 1.30 NA) objectives. Z-stacks at 2048 × 2048 pixels were collected at 0.2 or 0.3 µm (MCF-10A), 0.5 µm (MECs) and 1 µm (mammary sections) intervals. Images were processed with Fiji software [82]. Astral microtubule images were denoised using ND-Safir 3 software [83].

ANXA1, LGN and $G_{\alpha i1}$ profiles at the cell cortex of metaphase cells were measured in Fiji using a custom macro as described [84]. Fluorescent intensity values were reported along the cortex starting (and finishing) from a point facing the metaphase plate. Position 0 and 180 face the chromosome plate (central cortex) and position 90 and 270 face spindle poles (lateral cortex): 180 positions were scanned (every 2°) along the cortex. Profiles of ANXA1 and LGN at the cell cortex of prometaphase cells were measured similarly in Fiji with a custom macro (See Supplementary Information). To account for more elongated cell shapes, a line was drawn along the cell contour using the Freehand tool and the macro fits an ellipse to this contour. Fluorescent intensities were calculated along a 30 pixel-long radial line overlapping the cortex and the maximum intensity was reported. The whole cell contour was scanned at 180 successive positions (every 2°) starting (and finishing) at the ellipse's short axis assuming

the metaphase plate will align with the long axis of the ellipse. To compare signals from ANXA1 and LGN in prometaphase and metaphase cells, intensity values were corrected by subtracting background measurements. Average profiles were calculated from individual profiles.

Astral microtubule intensity (α-tubulin signal) was measured in Fiji. Maximum projections of images were generated and the fluorescence intensity of the whole cell (I_{total}) and the spindle ($I_{spindle}$) excluding spindle poles with astral microtubules were measured. Background signal was subtracted, and the relative fluorescence intensity of astral microtubules ($I_{astral,\ rel}$) was calculated as $I_{astral,\ rel} = (I_{total} - I_{spindle})/I_{spindle}$. Length of astral microtubules was measured by drawing a line along the astral microtubule extending towards the cell cortex on both sides of the poles. Similarly, the pole-to-cortex distance was measured by drawing a line towards the closest cell cortex in line with the spindle axis. Ratios were calculated by dividing the longer length or distance by the shorter length or distance.

Quantifications of number of lumen and shape descriptors (circularity, area/size, roundness), in MEC organoids were performed using Fiji. Organoids and lumen were outlined using the Fiji polygon selection tool, followed by shape descriptors extraction. Fluorescence intensities of E-cadherin and F-actin at the cell cortex were analysed using a semi-automated Fiji macro (Cell-o-Tape) [85]. Cell cortex were manually outlined using the Fiji segmented line tool in the E-cadherin channel, and signal intensities of the cellular perimeter were measured. Using the same perimeter, F-actin intensities were measured for the same cell. Graphic representation of both fluorescence intensities was performed by averaging the intensities of all cells per organoid.

Mitotic spindle orientation was measured using Fiji in metaphase cells stained for γ-tubulin (MCF-10A) or α-tubulin (organoid). In MCF-10A, the spindle axis was defined by drawing a 30-pixel wide line across both spindle poles and repositioned along the z axis. The spindle axis angle was measured in respect to the substratum using the angle tool. Similarly, the spindle axis angle in organoid was measured in respect to the plan of the basement membrane.

Quantitative live cell imaging

For live cell imaging, MCF-10A or GFP-LGN-expressing MCF-10A cells were plated in glass bottom dishes (Nunc). Prior to imaging, cells were incubated in cell culture media supplemented with 100 ng/ml Hoechst 33342 for 30 min. When mitotic spindles were observed, cells were further incubated in cell culture media supplemented with 100 nM SiR-tubulin (Spirochrome) for 3h. Cells were imaged at 37°C in CO_2 independent media (Gibco) using a DeltaVision Elite microscope (GE Healthcare) coupled to a sCMOS max chip area 2,048 x 2,048 camera (G.E. Healthcare). For each recording, image stacks of 30 to 40 planes at 0.6 µm increments were acquired using a PlanApo 60x/1.42 Oil immersion objective (Olympus) with 2x2 binning. Images were taken at 3 stage positions every 2.5 or 3 min for 3 or 5h. Exposure times were 250 msec and 5% laser power for GFP, 80 msec and 2% laser power for labelled DNA and 80 msec and 2% laser power for labelled microtubules using the DAPI-FITC-mCh-Cy5 filter set. Images were deconvolved using the DeltaVision software SoftWoRx and further processed using Fiji.

Mitotic spindle oscillations were calculated from time-lapse videos of MCF-10A cells labelled with SiR-tubulin and Hoechst 33342. Metaphase spindle angles in the z and xy plane were manually determined for every frame using Fiji. Measurements of the spindle angle axis in the z plane were performed as described above in fixed cells. Spindle angles were reported as positive values unless spindle poles changed direction. In this case, angles were displayed as negative values. Mitotic spindle orientation in the xy plane was measured by drawing a line crossing both spindle poles of the first frame of metaphase. This line was embedded to all the following frames to mark the initial position of the mitotic spindle. In the next frame, another line was overlaid across the poles to define the new spindle axis. The angle between the initial spindle position and the current spindle axis was measured using the angle tool. Spindle movement directions were considered by reporting spindle rotations clockwise as positive angles and reverse movements as negative angles. Spindle angle deviations > 10° between two frames were counted as oscillation events. The oscillation index was determined as the percentage of oscillation events in respect to the total number of frames.

Metaphase plates were tracked using IMARIS software (Bitplane). First, a maximum intensity z-projection was created. The DNA metaphase plates were segmented using the Surface module and the centre of the DNA was marked with a point. The movement of this centre point was then tracked automatically over time starting from the first frame of metaphase to the last before anaphase. Movement tracks in the xy plane were reported. Displacement length was the length of DNA displacement from starting point. Velocity was calculated by the total track length divided by tracking time (metaphase plate congression time).

Statistical analysis

Most of the experiments were repeated at least three times and the exact *n* is stated in the corresponding figure legend. Statistical significance of the overrepresentation of enriched proteins in biological processes and pathways were analysed with the ClueGO App (version 2.5.7) using hypergeometric test (Fisher's Exact Test) and the Bonferroni step-down correction method for multiple testing. Bar graphs of enrichment analyses were created using R statistical software (version 3.6.3) and RStudio (version 1.2.1335). All other statistical analysis were performed with GraphPad Prism 9.0 software. Multiple groups were tested using analysis of variance (ANOVA) with post hoc Tukey test, and comparisons between two groups were performed using *t*-tests. Data are shown as mean ± standard error of the mean (s.e.m.). $P \leq 0.05$ was considered statistically significant. Asterisks indicate levels of significance (* $P \leq 0.05$; ** $P \leq 0.01$; *** $P \leq 0.001$; **** $P \leq 0.0001$). The experiments were not randomized. The investigators were not blinded to allocation during experiments and outcome assessment.

Acknowledgments

We would like to thank Dr Mark Willett for valuable assistance with fluorescence microscopy; Andrew Crocker for mouse husbandry; Dr Melissa Andrews for providing the HEK293 cell line; Dr David Bryant for providing the pLKO.4-Mem-Venus lentiviral plasmid. In addition, we thank Dr Marcin Przewloka for critically reviewing the manuscript. This work was supported by a Wellcome Trust Seed Award in Science (210077/Z/17/Z) and MRC New Investigator Research Grant (MR/R026610/1) awarded to SE. MF was supported by a Gerald Kerkut Trust PhD studentship.

Author contributions

MF designed and performed most of the experiments, analysed, and interpreted the data. FSGH performed the bioinformatic analyses. MMH performed immunofluorescence and 3D culture experiments. LM and CLGJS analysed 3D culture data. XM designed custom macros for the quantification of cortical fluorescence intensities. PS performed the LC-MS/MS experiments. SE conceived and designed the project, performed experiments, analysed, and interpreted the data, and wrote the manuscript. All the authors provided intellectual input, edited, and approved the final manuscript.

Competing interests

The authors declare no competing financial interests.

Data availability

All the data that support the findings of this study are available within the paper and its supplementary information files. Further information and requests for all other relevant data and reagents are available from the corresponding author upon reasonable request. The mass spectrometry proteomics data have been deposited the ProteomeXchange Consortium via the PRIDE partner repository [29] with the dataset identifier PXD027452.

References

1. Morin, X. & Bellaiche, Y. Mitotic spindle orientation in asymmetric and symmetric cell divisions during animal development. *Dev Cell* **21**, 102-119 (2011).

2. Mukherjee, S., Kong, J. & Brat, D.J. Cancer stem cell division: when the rules of asymmetry are broken. *Stem Cells Dev* **24**, 405-416 (2015).

3. Santoro, A., Vlachou, T., Carminati, M., Pelicci, P.G. & Mapelli, M. Molecular mechanisms of asymmetric divisions in mammary stem cells. *EMBO Rep* **17**, 1700-1720 (2016).

4. di Pietro, F., Echard, A. & Morin, X. Regulation of mitotic spindle orientation: an integrated view. *EMBO Rep* **17**, 1106-1130 (2016).

5. Kiyomitsu, T. The cortical force-generating machinery: how cortical spindle-pulling forces are generated. *Curr Opin Cell Biol* **60**, 1-8 (2019).

6. Kiyomitsu, T. & Cheeseman, I.M. Chromosome- and spindle-pole-derived signals generate an intrinsic code for spindle position and orientation. *Nat Cell Biol* **14**, 311-317 (2012).

7. Bergstralh, D.T., Dawney, N.S. & St Johnston, D. Spindle orientation: a question of complex positioning. *Development* **144**, 1137-1145 (2017).

8. Schaefer, M., Shevchenko, A., Shevchenko, A. & Knoblich, J.A. A protein complex containing Inscuteable and the Galpha-binding protein Pins orients asymmetric cell divisions in Drosophila. *Curr Biol* **10**, 353-362 (2000).

9. Yu, F., Morin, X., Cai, Y., Yang, X. & Chia, W. Analysis of partner of inscuteable, a novel player of Drosophila asymmetric divisions, reveals two distinct steps in inscuteable apical localization. *Cell* **100**, 399-409 (2000).

10. Williams, S.E., Ratliff, L.A., Postiglione, M.P., Knoblich, J.A. & Fuchs, E. Par3-mInsc and Galphai3 cooperate to promote oriented epidermal cell divisions through LGN. *Nat Cell Biol* **16**, 758-769 (2014).

11. Hao, Y. *et al.* Par3 controls epithelial spindle orientation by aPKC-mediated phosphorylation of apical Pins. *Curr Biol* **20**, 1809-1818 (2010).

12. Woodard, G.E. *et al.* Ric-8A and Gi alpha recruit LGN, NuMA, and dynein to the cell cortex to help orient the mitotic spindle. *Mol Cell Biol* **30**, 3519-3530 (2010).

13. Carminati, M. *et al.* Concomitant binding of Afadin to LGN and F-actin directs planar spindle orientation. *Nat Struct Mol Biol* **23**, 155-163 (2016).

14. Wang, X. *et al.* E-cadherin bridges cell polarity and spindle orientation to ensure prostate epithelial integrity and prevent carcinogenesis in vivo. *PLoS Genet* **14**, e1007609 (2018).

15. Gloerich, M., Bianchini, J.M., Siemers, K.A., Cohen, D.J. & Nelson, W.J. Cell division orientation is coupled to cell-cell adhesion by the E-cadherin/LGN complex. *Nat Commun* **8**, 13996 (2017).

16. Porter, A.P., White, G.R.M., Mack, N.A. & Malliri, A. The interaction between CASK and the tumour suppressor Dlg1 regulates mitotic spindle orientation in mammalian epithelia. *J Cell Sci* **132** (2019).

17. Matsumura, S. *et al.* ABL1 regulates spindle orientation in adherent cells and mammalian skin. *Nat Commun* **3**, 626 (2012).

18. Chiu, C.W.N. *et al.* SAPCD2 Controls Spindle Orientation and Asymmetric Divisions by Negatively Regulating the Galphai-LGN-NuMA Ternary Complex. *Dev Cell* **36**, 50-62 (2016).

19. Fu, N.Y., Nolan, E., Lindeman, G.J. & Visvader, J.E. Stem Cells and the Differentiation Hierarchy in Mammary Gland Development. *Physiol Rev* **100**, 489-523 (2020).

20. Taddei, I. *et al.* Beta1 integrin deletion from the basal compartment of the mammary epithelium affects stem cells. *Nat Cell Biol* **10**, 716-722 (2008).

21. Regan, J.L. *et al.* Aurora A kinase regulates mammary epithelial cell fate by determining mitotic spindle orientation in a Notch-dependent manner. *Cell Rep* **4**, 110-123 (2013).

22. Elias, S. *et al.* Huntingtin regulates mammary stem cell division and differentiation. *Stem Cell Reports* **2**, 491-506 (2014).

23. Villegas, E. *et al.* Plk2 regulates mitotic spindle orientation and mammary gland development. *Development* **141**, 1562-1571 (2014).

24. Morris, E.J., Gillespie, J.A., Maxwell, C.A. & Dedhar, S. A Model of Differential Mammary Growth Initiation by Stat3 and Asymmetric Integrin-alpha6 Inheritance. *Cell Rep* **30**, 3605-3615 e3605 (2020).

25. Ballard, M.S. *et al.* Mammary Stem Cell Self-Renewal Is Regulated by Slit2/Robo1 Signaling through SNAI1 and mINSC. *Cell Rep* **13**, 290-301 (2015).

26. Segatto, I. *et al.* Stathmin Is Required for Normal Mouse Mammary Gland Development and Delta16HER2-Driven Tumorigenesis. *Cancer Res* **79**, 397-409 (2019).

27. Santoro, A. *et al.* p53 Loss in Breast Cancer Leads to Myc Activation, Increased Cell Plasticity, and Expression of a Mitotic Signature with Prognostic Value. *Cell Rep* **26**, 624-638 e628 (2019).

28. Foo, S.L., Yap, G., Cui, J. & Lim, L.H.K. Annexin-A1 - A Blessing or a Curse in Cancer? *Trends Mol Med* **25**, 315-327 (2019).

29. Perez-Riverol, Y. *et al.* The PRIDE database and related tools and resources in 2019: improving support for quantification data. *Nucleic Acids Res* **47**, D442-D450 (2019).

30. Mellacheruvu, D. *et al.* The CRAPome: a contaminant repository for affinity purification-mass spectrometry data. *Nat Methods* **10**, 730-736 (2013).

31. Liu, X.S. *et al.* Plk1 phosphorylates Sgt1 at the kinetochores to promote timely kinetochore-microtubule attachment. *Mol Cell Biol* **32**, 4053-4067 (2012).

32. Busson, S., Dujardin, D., Moreau, A., Dompierre, J. & De Mey, J.R. Dynein and dynactin are localized to astral microtubules and at cortical sites in mitotic epithelial cells. *Curr Biol* **8**, 541-544 (1998).

33. Zheng, Z. *et al.* Evidence for dynein and astral microtubule-mediated cortical release and transport of Galphai/LGN/NuMA complex in mitotic cells. *Mol Biol Cell* **24**, 901-913 (2013).

34. Okumura, M., Natsume, T., Kanemaki, M.T. & Kiyomitsu, T. Dynein-Dynactin-NuMA clusters generate cortical spindle-pulling forces as a multi-arm ensemble. *Elife* **7** (2018).

35. Yang, Z., Tulu, U.S., Wadsworth, P. & Rieder, C.L. Kinetochore dynein is required for chromosome motion and congression independent of the spindle checkpoint. *Curr Biol* **17**, 973-980 (2007).

36. Musacchio, A. The Molecular Biology of Spindle Assembly Checkpoint Signaling Dynamics. *Curr Biol* **25**, R1002-1018 (2015).

37. Maiato, H., Rieder, C.L., Earnshaw, W.C. & Sunkel, C.E. How do kinetochores CLASP dynamic microtubules? *Cell Cycle* **2**, 511-514 (2003).

38. Pereira, A.L. *et al.* Mammalian CLASP1 and CLASP2 cooperate to ensure mitotic fidelity by regulating spindle and kinetochore function. *Mol Biol Cell* **17**, 4526-4542 (2006).

39. Bird, S.L., Heald, R. & Weis, K. RanGTP and CLASP1 cooperate to position the mitotic spindle. *Mol Biol Cell* **24**, 2506-2514 (2013).

40. David, A.F. *et al.* Augmin accumulation on long-lived microtubules drives amplification and kinetochore-directed growth. *J Cell Biol* **218**, 2150-2168 (2019).

41. Bouissou, A. *et al.* gamma-Tubulin Ring Complexes and EB1 play antagonistic roles in microtubule dynamics and spindle positioning. *EMBO J* **33**, 114-128 (2014).

42. Mishra, R.K., Chakraborty, P., Arnaoutov, A., Fontoura, B.M. & Dasso, M. The Nup107-160 complex and gamma-TuRC regulate microtubule polymerization at kinetochores. *Nat Cell Biol* **12**, 164-169 (2010).

43. Singh, D., Schmidt, N., Muller, F., Bange, T. & Bird, A.W. Destabilization of Long Astral Microtubules via Cdk1-Dependent Removal of GTSE1 from Their Plus Ends Facilitates Prometaphase Spindle Orientation. *Curr Biol* **31**, 766-781 e768 (2021).

44. Sillje, H.H., Nagel, S., Korner, R. & Nigg, E.A. HURP is a Ran-importin beta-regulated protein that stabilizes kinetochore microtubules in the vicinity of chromosomes. *Curr Biol* **16**, 731-742 (2006).

45. Wilde, A. & Zheng, Y. Stimulation of microtubule aster formation and spindle assembly by the small GTPase Ran. *Science* **284**, 1359-1362 (1999).

46. Grzmil, M. *et al.* An oncogenic role of eIF3e/INT6 in human breast cancer. *Oncogene* **29**, 4080-4089 (2010).

47. Morris, C. & Jalinot, P. Silencing of human Int-6 impairs mitosis progression and inhibits cyclin B-Cdk1 activation. *Oncogene* **24**, 1203-1211 (2005).

48. Flower, R.J. & Blackwell, G.J. Anti-inflammatory steroids induce biosynthesis of a phospholipase A2 inhibitor which prevents prostaglandin generation. *Nature* **278**, 456-459 (1979).

49. Watanabe, M., Ando, Y., Todoroki, H., Minami, H. & Hidaka, H. Molecular cloning and sequencing of a cDNA clone encoding a new calcium binding protein, named calgizzarin, from rabbit lung. *Biochem Biophys Res Commun* **181**, 644-649 (1991).

50. De Buck, M. *et al.* Structure and Expression of Different Serum Amyloid A (SAA) Variants and their Concentration-Dependent Functions During Host Insults. *Curr Med Chem* **23**, 1725-1755 (2016).

51. Perretti, M. & D'Acquisto, F. Annexin A1 and glucocorticoids as effectors of the resolution of inflammation. *Nat Rev Immunol* **9**, 62-70 (2009).

52. Lukinavicius, G. *et al.* Fluorogenic probes for live-cell imaging of the cytoskeleton. *Nat Methods* **11**, 731-733 (2014).

53. Peyre, E. *et al.* A lateral belt of cortical LGN and NuMA guides mitotic spindle movements and planar division in neuroepithelial cells. *J Cell Biol* **193**, 141-154 (2011).

54. Williams, S.E., Beronja, S., Pasolli, H.A. & Fuchs, E. Asymmetric cell divisions promote Notch-dependent epidermal differentiation. *Nature* **470**, 353-358 (2011).

55. Zheng, Z. *et al.* LGN regulates mitotic spindle orientation during epithelial morphogenesis. *J Cell Biol* **189**, 275-288 (2010).

56. Ahmed, M.I., Elias, S., Mould, A.W., Bikoff, E.K. & Robertson, E.J. The transcriptional repressor Blimp1 is expressed in rare luminal progenitors and is essential for mammary gland development. *Development* **143**, 1663-1673 (2016).

57. McCaffrey, L.M. & Macara, I.G. Epithelial organization, cell polarity and tumorigenesis. *Trends Cell Biol* **21**, 727-735 (2011).

58. Tame, M.A., Raaijmakers, J.A., Afanasyev, P. & Medema, R.H. Chromosome misalignments induce spindle-positioning defects. *EMBO Rep* **17**, 317-325 (2016).

59. Howell, B.J. *et al.* Cytoplasmic dynein/dynactin drives kinetochore protein transport to the spindle poles and has a role in mitotic spindle checkpoint inactivation. *J Cell Biol* **155**, 1159-1172 (2001).

60. Guo, H., Wei, J.H., Zhang, Y. & Seemann, J. Importin alpha phosphorylation promotes TPX2 activation by GM130 to control astral microtubules and spindle orientation. *J Cell Sci* **134** (2021).

61. Yu, H. *et al.* NDP52 tunes cortical actin interaction with astral microtubules for accurate spindle orientation. *Cell Res* **29**, 666-679 (2019).

62. Dogterom, M. & Koenderink, G.H. Actin-microtubule crosstalk in cell biology. *Nat Rev Mol Cell Biol* **20**, 38-54 (2019).

63. Glenney, J.R., Jr., Tack, B. & Powell, M.A. Calpactins: two distinct Ca++-regulated phospholipid- and actin-binding proteins isolated from lung and placenta. *J Cell Biol* **104**, 503-511 (1987).

64. Rintala-Dempsey, A.C., Rezvanpour, A. & Shaw, G.S. S100-annexin complexes--structural insights. *FEBS J* **275**, 4956-4966 (2008).

65. Jaiswal, J.K. *et al.* S100A11 is required for efficient plasma membrane repair and survival of invasive cancer cells. *Nat Commun* **5**, 3795 (2014).

66. Alvarez-Martinez, M.T. *et al.* Characterization of the interaction between annexin I and profilin. *Eur J Biochem* **238**, 777-784 (1996).

67. Alvarez-Martinez, M.T., Porte, F., Liautard, J.P. & Sri Widada, J. Effects of profilin-annexin I association on some properties of both profilin and annexin I: modification of the inhibitory activity of profilin on actin polymerization and inhibition of the self-association of annexin I and its interactions with liposomes. *Biochim Biophys Acta* **1339**, 331-340 (1997).

68. Xiao, Y. *et al.* Annexin A1 can inhibit the in vitro invasive ability of nasopharyngeal carcinoma cells possibly through Annexin A1/S100A9/Vimentin interaction. *PLoS One* **12**, e0174383 (2017).

69. Duarte, S. *et al.* Vimentin filaments interact with the actin cortex in mitosis allowing normal cell division. *Nat Commun* **10**, 4200 (2019).

70. Serres, M.P. *et al.* F-Actin Interactome Reveals Vimentin as a Key Regulator of Actin Organization and Cell Mechanics in Mitosis. *Dev Cell* **52**, 210-222 e217 (2020).

71. Chishiki, K., Kamakura, S., Hayase, J. & Sumimoto, H. Ric-8A, an activator protein of Galphai, controls mammalian epithelial cell polarity for tight junction assembly and cystogenesis. *Genes Cells* **22**, 293-309 (2017).

72. Lazaro-Dieguez, F. *et al.* Par1b links lumen polarity with LGN-NuMA positioning for distinct epithelial cell division phenotypes. *J Cell Biol* **203**, 251-264 (2013).

73. Granit, R.Z. *et al.* Regulation of Cellular Heterogeneity and Rates of Symmetric and Asymmetric Divisions in Triple-Negative Breast Cancer. *Cell Rep* **24**, 3237-3250 (2018).

74. Allred, D.C. Issues and updates: evaluating estrogen receptor-alpha, progesterone receptor, and HER2 in breast cancer. *Mod Pathol* **23 Suppl 2**, S52-59 (2010).

75. Schenborn, E.T. & Goiffon, V. Calcium Phosphate Transfection of Mammalian Cultured Cells, in *Transcription Factor Protocols*. (ed. M.J. Tymms) 135-145 (Humana Press, Totowa, NJ; 2000).

76. McCaffrey, L.M. & Macara, I.G. The Par3/aPKC interaction is essential for end bud remodeling and progenitor differentiation during mammary gland morphogenesis. *Genes Dev* **23**, 1450-1460 (2009).

77. Hubner, N.C. & Mann, M. Extracting gene function from protein-protein interactions using Quantitative BAC InteraCtomics (QUBIC). *Methods* **53**, 453-459 (2011).

78. Smits, A.H., Jansen, P.W., Poser, I., Hyman, A.A. & Vermeulen, M. Stoichiometry of chromatin-associated protein complexes revealed by label-free quantitative mass spectrometry-based proteomics. *Nucleic Acids Res* **41**, e28 (2013).

79. Szklarczyk, D. *et al.* STRING v11: protein-protein association networks with increased coverage, supporting functional discovery in genome-wide experimental datasets. *Nucleic Acids Res* **47**, D607-D613 (2019).

80. Shannon, P. *et al.* Cytoscape: a software environment for integrated models of biomolecular interaction networks. *Genome Res* **13**, 2498-2504 (2003).

81. Bindea, G. *et al.* ClueGO: a Cytoscape plug-in to decipher functionally grouped gene ontology and pathway annotation networks. *Bioinformatics* **25**, 1091-1093 (2009).

82. Schindelin, J. *et al.* Fiji: an open-source platform for biological-image analysis. *Nat Methods* **9**, 676-682 (2012).

83. Boulanger, J. *et al.* Patch-based nonlocal functional for denoising fluorescence microscopy image sequences. *IEEE Trans Med Imaging* **29**, 442-454 (2010).

84. di Pietro, F. *et al.* An RNAi Screen in a Novel Model of Oriented Divisions Identifies the Actin-Capping Protein Z beta as an Essential Regulator of Spindle Orientation. *Curr Biol* **27**, 2452-2464 e2458 (2017).

85. French, A.P. *et al.* Identifying biological landmarks using a novel cell measuring image analysis tool: Cell-o-Tape. *Plant Methods* **8**, 7 (2012).

Figure 1

Fankhaenel *et al.*

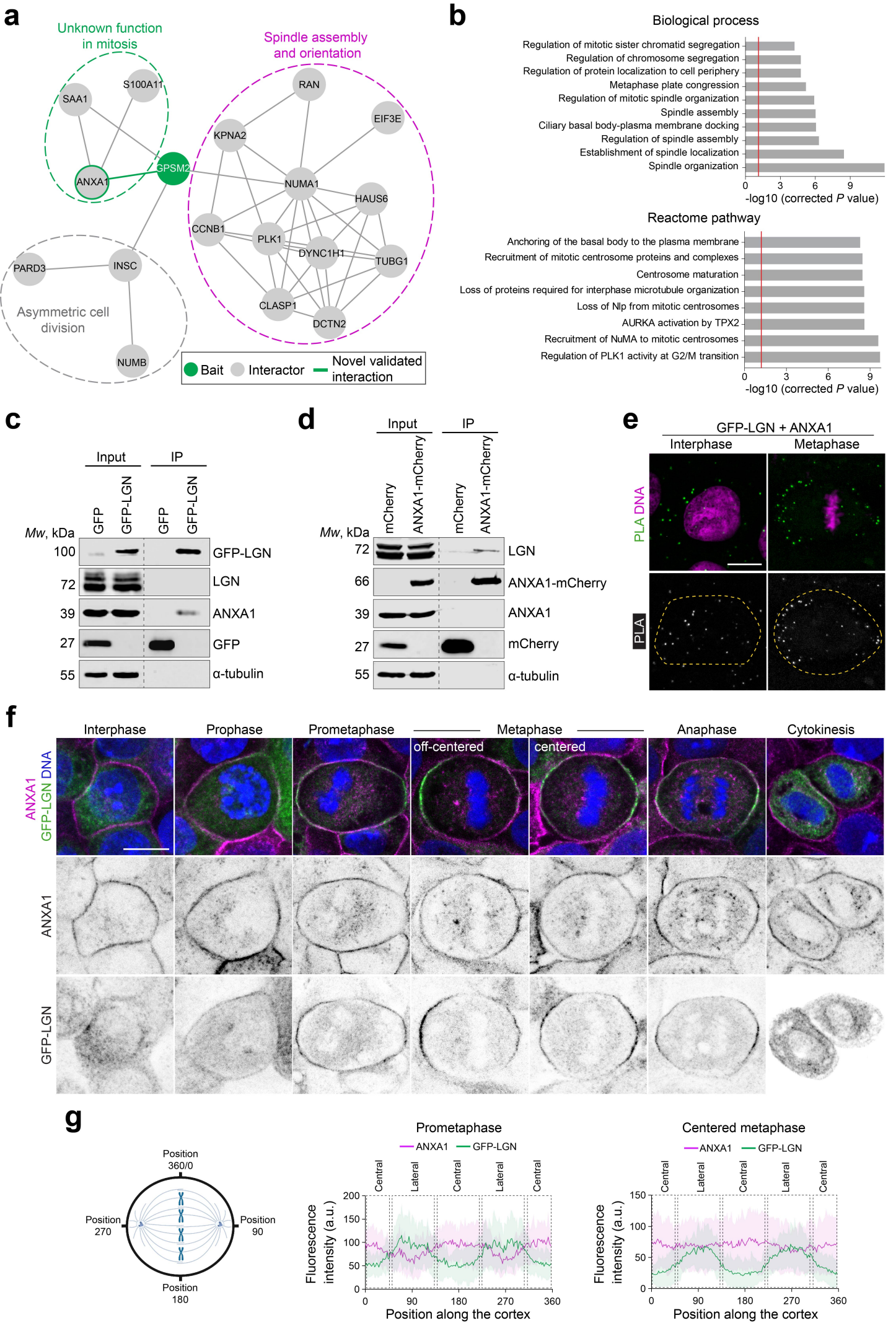

Figure 1 ANXA1 interacts with LGN at the cell cortex during mitosis. (a) Protein-protein interaction network of LGN (GPSM2, red) showing several interactors (grey) of known and unknown mitotic functions. The green line highlights a novel interaction between LGN and ANXA1, which is further validated in this study. **(b)** Gene Ontology analysis of the LGN network presenting terms from Biological process (left) and Reactome pathway analysis (right) significantly enriched. *P*-values were derived from the hypergeometric test (Fisher's Exact Test) with Bonferroni step-down correction from multiple tests. **(c)** ANXA1 and GFP-LGN co-immunoprecipitate from clonal MCF-10A stably expressing GFP-LGN, arrested in metaphase. Lysates were subjected to affinity purification with GFP-Trap beads. The immunoprecipitates (IP) were analysed by western blotting. **(d)** LGN and ANXA1-mCherry co-immunoprecipitate from clonal MCF-10A cells stably expressing ANXA1-mCherry, arrested in metaphase. Lysates were subjected to affinity purification with RFP-Trap beads. The immunoprecipitates were analysed by western blotting. **(e)** Proximity ligation assay (PLA) performed using GFP and ANXA1 antibodies in GFP-LGN-expressing MCF10A cells. Cells were counterstained with DAPI (DNA, magenta). Green dotted lines indicate the cell contour. **(f)** Confocal images of representative clonal MCF-10A cells stably expressing GFP-LGN (green) stained for ANXA1 (magenta) and counterstained with DAPI (DNA, blue). **(g)** Average cortical fluorescence intensity profiles of GFP-LGN and ANXA1 in prometaphase cells (left) and metaphase cells (right) from 3 independent experiments (prometaphase n = 33 cells; metaphase n = 36 cells). Positions along the cortex in the graphs correspond to coordinates as illustrated in the schematic. All scale bars, 10 μm.

Figure 2

Fankhaenel *et al.*

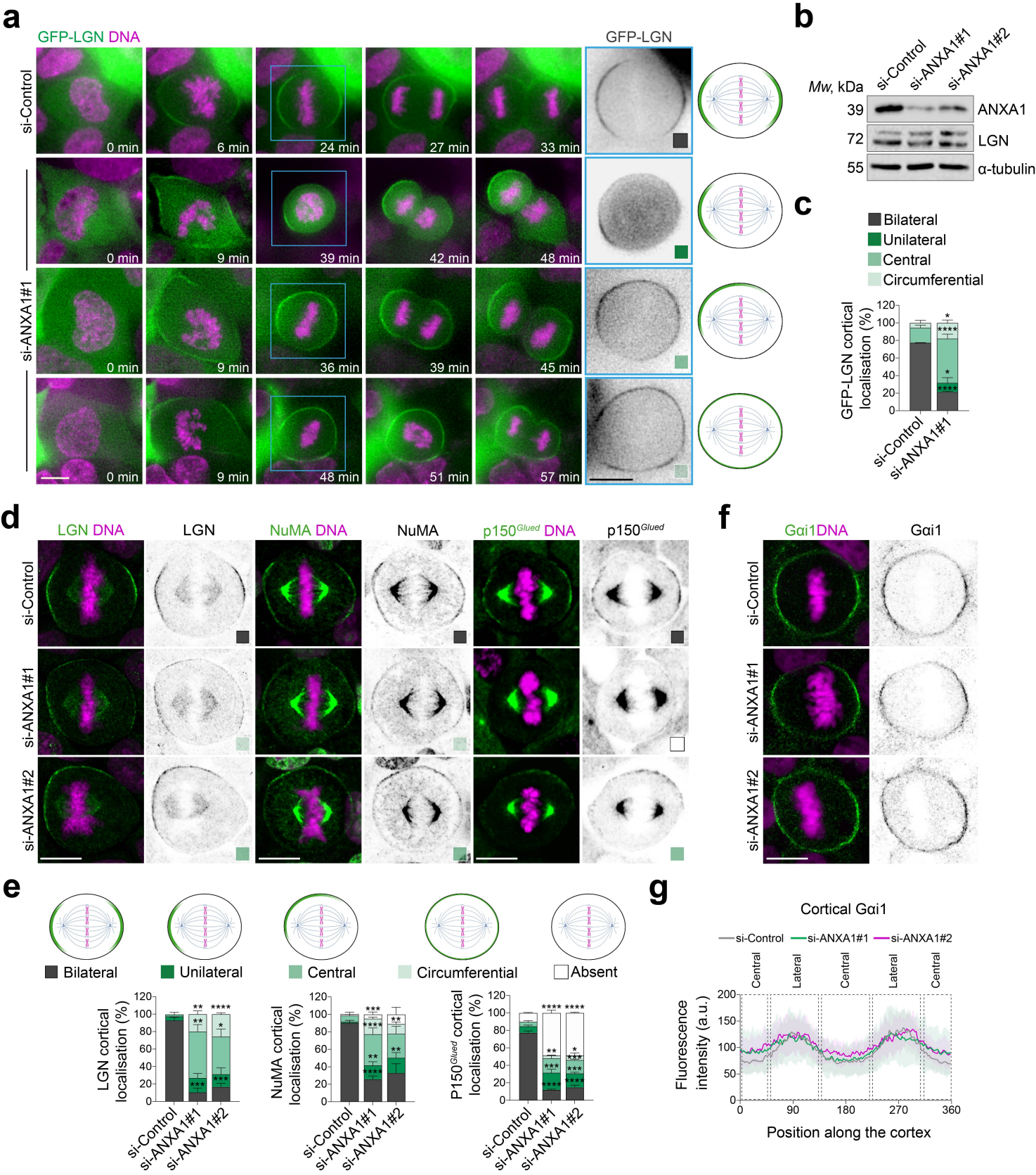

Figure 2 ANXA1 is required for correct localisation of the LGN-NuMA-Dynein-Dynactin complex at the cell cortex during mitosis. (a) Left: time-lapse images of representative clonal MCF-10A cells stably expressing GFP-LGN (green), treated with si-Control or si-ANXA1#1. DNA is stained with Hoechst 33342 (magenta) 30 min before imaging. Right: illustration showing the observed cortical localisation of GFP-LGN **(b)** Western blotting of extracts from siRNA-transfected cells. **(c)** Percentage of cortical localisation of GFP-LGN in siRNA-transfected cells (si-Control: n = 53 cells; si-ANXA1#1: n = 41 cells). **(d)** Confocal images of representative si-Control- and si-ANXA1#1-transfected metaphase cells stained for LGN, NuMA or $p150^{Glued}$ (green) and counterstained with DAPI (DNA, magenta). **(e)** Left: percentage of cortical localisation of LGN, NuMA or $p150^{Glued}$ in siRNA-transfected metaphase cells: LGN (si-Control: n = 70 cells; si-ANXA1: n = 51 cells; si-ANXA1#2: n = 43 cells), NuMA (si-Control n = 73; si-ANXA1 n = 62; si-ANXA1#2 n = 45), $p150^{Glued}$ (si-Control n = 79; si-ANXA1 n = 101; si-ANXA1#2 n = 99). **(f)** Confocal images of representative si-Control-, si-ANXA1#1- and si-ANXA1#2-treated metaphase cells stained for $G_{\alpha i1}$ (green) and counterstained with DAPI (DNA, magenta). **(g)** Average cortical fluorescence intensity profiles of $G_{\alpha i1}$ in siRNA-transfected metaphase cells (si-Control: n = 32; si-ANXA1#1: n = 30; si-ANXA1#2: n = 30). All data are presented as means ± s.e.m. from 3 independent experiments. * $P \leq 0.05$, ** $P \leq 0.01$, **** $P \leq 0.0001$ (one-way ANOVA; *t*-test). All scale bars, 10 μm.

Figure 3 Fankhaenel *et al.*

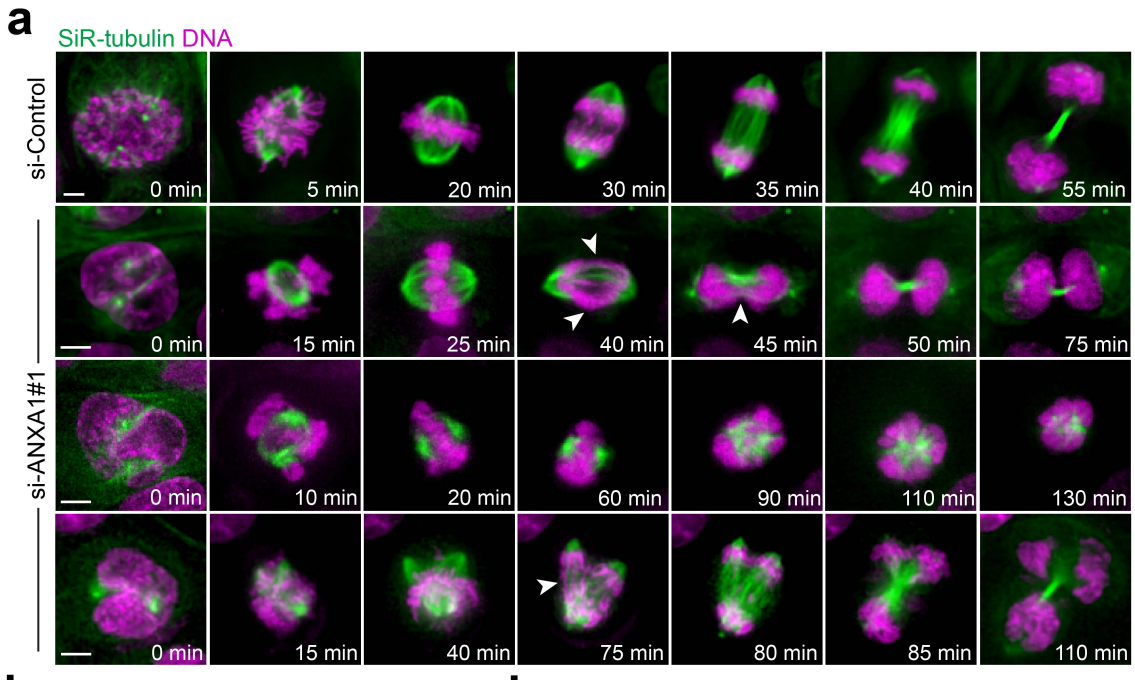

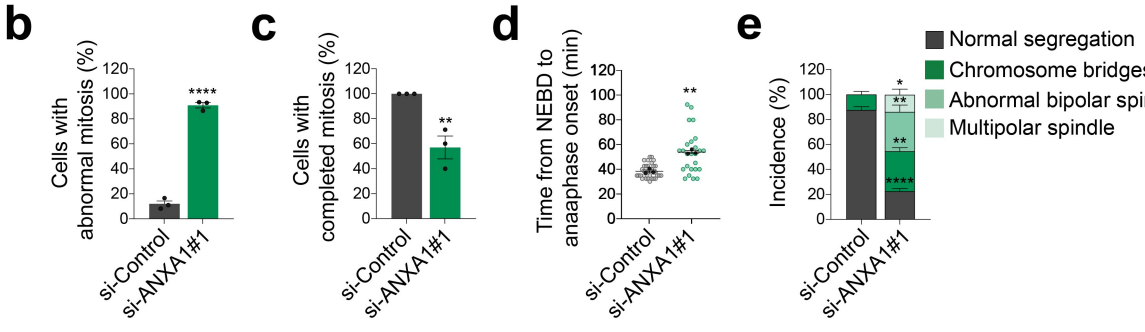

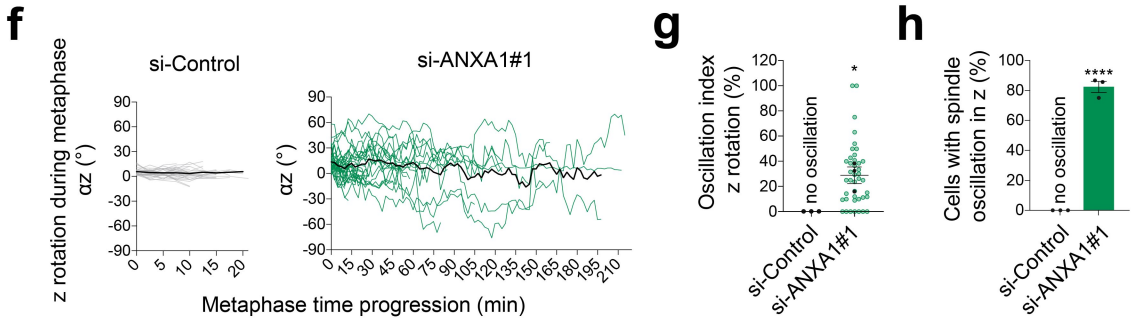

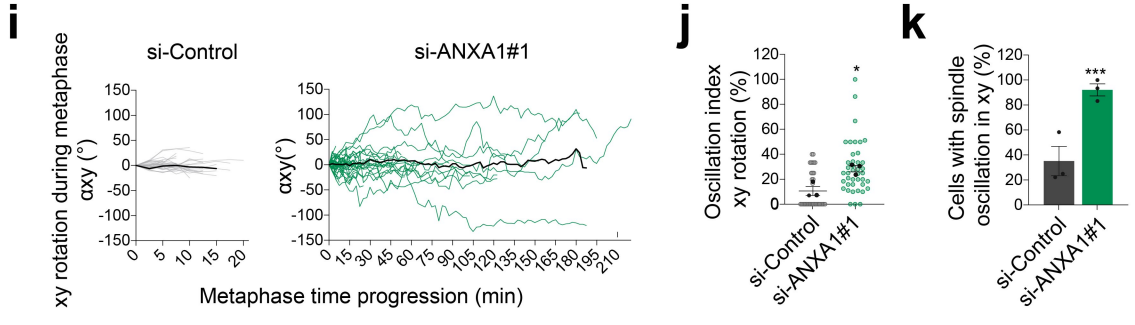

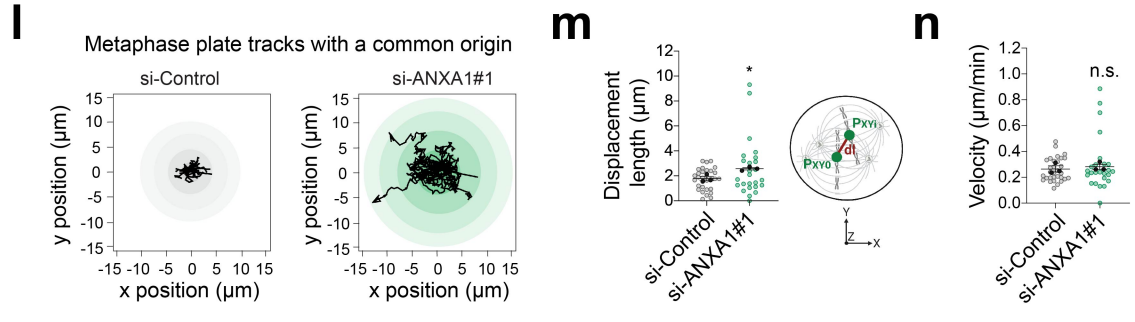

Figure 3 ANXA1 is required for correct mitotic progression and spindle dynamics. (a) Time-lapse images of representative MCF-10A cells treated with si-Control or si-ANXA1#1. Microtubules are labelled with SiR-tubulin (green) and DNA with Hoechst 33342 (magenta), 2h and 30 min before acquisition, respectively. Scale bars, 5 µm. **(b)** Percentage of cells with abnormal mitosis in siRNA-transfected cells. **(c)** Percentage of cells that completed mitosis in siRNA-treated cells. **(d)** Time from nuclear envelope breakdown (NEBD) to anaphase onset in siRNA-transfected cells. **(e)** Percentage of chromosomes segregation and spindle assembly defects in siRNA-transfected cells. **(f)** Dynamics of z orientation (αz) during metaphase in si-Control- (left) and si-ANXA1#1-treated (right) cells. Black lines represent the average spindle angles of all analysed cells. **(g)** Oscillation index in siRNA-transfected cells, representing the frequency at which mitotic spindle position changes > 10° between two successive frames in the z axis. **(h)** Percentage of cells with spindle oscillations in the z axis in siRNA-transfected cells. **(i)** Dynamics of xy orientation (αxy) during metaphase in si-Control- (left) and si-ANXA1#1-transfected (right) cells. Black lines represent the average spindle angles of all analysed cells. **(j)** Oscillation index in si-Control- and si-ANXA1#1-transfected cells, representing the frequency at which mitotic spindle position changes > 10° between two successive frames in the xy axis. **(k)** Percentage of cells with spindle oscillations in the xy axis in siRNA-transfected cells. **(l)** Origin-aligned metaphase plate tracks in the xy plane of si-Control- (left) and si-ANXA1#1-transfected (right) cells. Black lines correspond to individual cells. **(m)** Displacement length from the starting point to the position at the end of metaphase in siRNA-transfected cells. **(n)** Velocity of metaphase plate movements in si-RNA-transfected, calculated by dividing the track length by metaphase duration. All data are presented as means ± s.e.m. from 3 independent experiments (si-Control: n = 33 cells; si-ANXA1#1: n = 44; si-ANXA1#2: n = 35 cells). * $P \leq 0.05$, ** $P \leq 0.01$, **** $P \leq 0.0001$ (*t*-test).

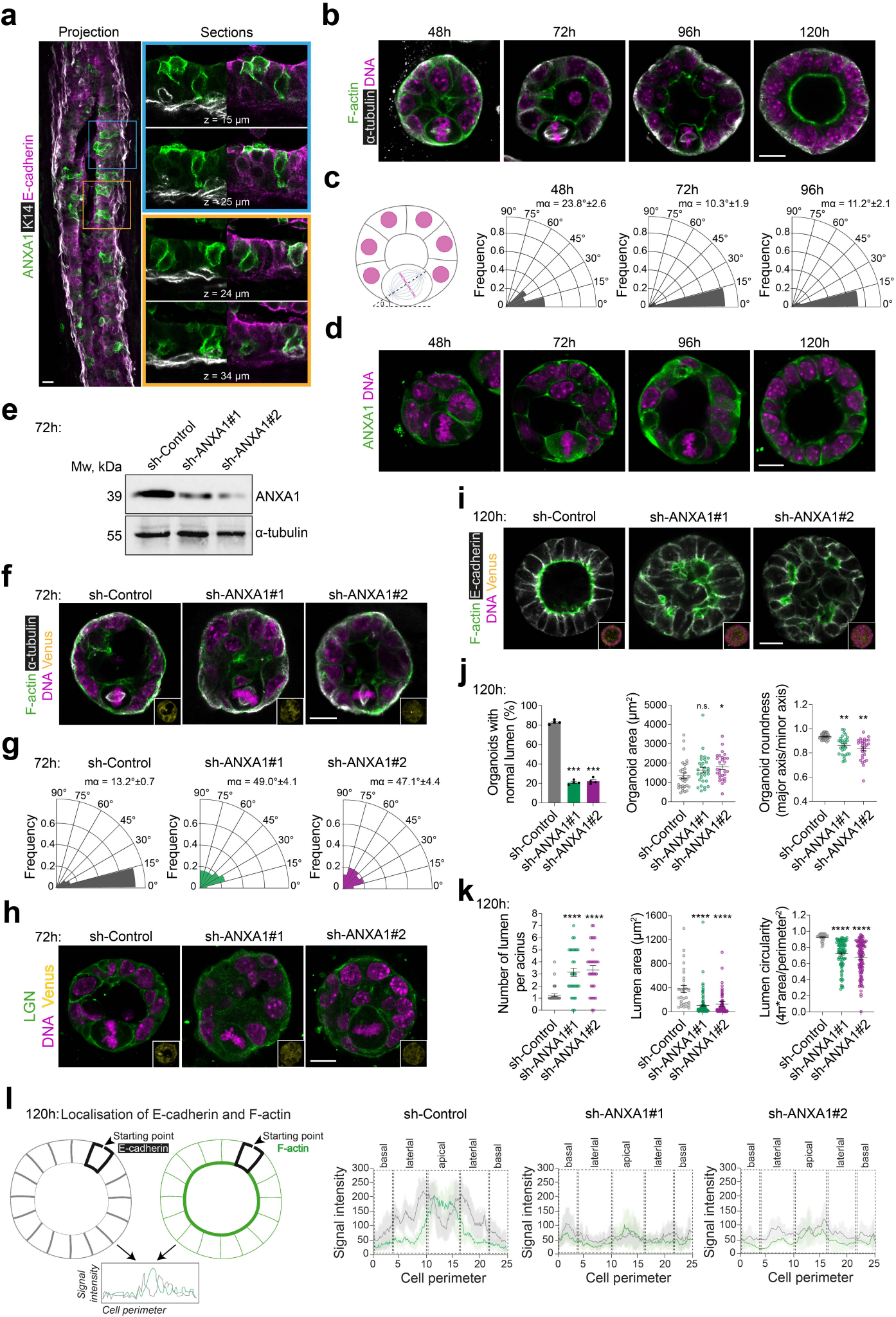
a
Projection
Sections
ANXA1 K14 E-cadherin
z = 15 µm
z = 25 µm
z = 24 µm
z = 34 µm
b
48h
72h
96h
120h
F-actin DNA
α-tubulin
c
48h
72h
96h
mα = 23.8°±2.6
mα = 10.3°±1.9
mα = 11.2°±2.1
Frequency
d
48h
72h
96h
120h
ANXA1 DNA
e
72h:
sh-Control
sh-ANXA1#1
sh-ANXA1#2
Mw, kDa
39
55
ANXA1
α-tubulin
f
72h:
sh-Control
sh-ANXA1#1
sh-ANXA1#2
F-actin α-tubulin
DNA Venus
g
72h:
sh-Control
sh-ANXA1#1
sh-ANXA1#2
mα = 13.2°±0.7
mα = 49.0°±4.1
mα = 47.1°±4.4
Frequency
h
72h:
sh-Control
sh-ANXA1#1
sh-ANXA1#2
LGN
DNA Venus
i
120h:
sh-Control
sh-ANXA1#1
sh-ANXA1#2
F-actin E-cadherin
DNA Venus
j
120h:
Organoids with normal lumen (%)
Organoid area (µm²)
Organoid roundness (major axis/minor axis)
n.s.
*
**
***
sh-Control
sh-ANXA1#1
sh-ANXA1#2
k
120h:
Number of lumen per acinus
Lumen area (µm²)
Lumen circularity (4π*area/perimeter²)
****
sh-Control
sh-ANXA1#1
sh-ANXA1#2
l
120h: Localisation of E-cadherin and F-actin
Starting point
E-cadherin
Starting point
F-actin
Signal intensity
Cell perimeter
sh-Control
sh-ANXA1#1
sh-ANXA1#2
basal
laterial
apical
laterial
basal
Signal intensity
Cell perimeter

Figure 4 ANXA1 is required for correct mitotic spindle orientation during 3D morphogenesis. (a) Confocal images of representative mouse mammary gland cryosections (50 µm-thick) stained for ANXA1 (green), K14 (grey) and E-cadherin (magenta). **(b)** Confocal images of representative MEC organoids stained for F-actin (green) and α-tubulin (grey) and counterstained with DAPI (DNA, magenta). **(c)** Spindle angle frequencies and mean angles (mα) (48h: n = 42 organoids; 72h: n = 40 organoids; 96h: n = 39 organoids). **(d)** Confocal images of representative organoids stained for ANXA1 (green) and counterstained with DAPI (DNA, magenta). **(e)** Western blotting of extracts from shRNA-transduced organoids. **(f)** Confocal images of representative shRNA-transduced organoids (Venus, yellow) stained for F-actin (green) and α-tubulin (grey) and counterstained with DAPI (DNA, magenta). **(g)** Spindle angle frequencies and mean angles (mα) (sh-Control: n = 30 organoids; sh-ANXA1#1: n = 30 organoids; sh-ANXA1#2: n = 30 organoids). **(h)** Confocal images of representative shRNA-transduced organoids (Venus, yellow) stained for LGN (green) and counterstained with DAPI (DNA, magenta). **(i)** Confocal images of representative shRNA-transduced organoids (Venus, yellow) stained for F-actin (green) and E-cadherin (grey) and counterstained with DAPI (DNA, magenta). **(j)** Quantification of the percentage of organoids with normal lumen (left) (sh-Control: n = 163 organoids; sh-ANXA1#1: n = 142 organoids; sh-ANXA1#2: n = 168 organoids), organoid area (middle) and organoid roundness (right) (sh-Control: n = 30 organoids; sh-ANXA1#1: n = 30 organoids; sh-ANXA1#2: n = 30 organoids). **(k)** Quantification of the number of lumen per organoid (left), lumen area (middle) and lumen circularity (right) (sh-Control n = 30; sh-ANXA1#1 n = 30; sh-ANXA1#2 n = 30). **(l)** Left: illustration showing quantification of cortical fluorescence intensity of F-actin (green) and E-cadherin (grey) in organoids. Right: average cortical fluorescence intensity profiles of E-cadherin and F-actin (sh-Control n = 30; sh-ANXA1#1 n = 30; sh-ANXA1#2 n = 30). All time-points of 3D culture are indicated in hours (h). All data are presented as means ± s.e.m. from at least 3 independent experiments. * $P \leq 0.05$, ** $P \leq 0.01$, *** $P \leq 0.001$ **** $P \leq 0.0001$ (Kolmogorov-Smirnov test; one-way ANOVA; *t*-test). All scale bars, 10 µm.

Figure 5

Fankhaenel *et al.*

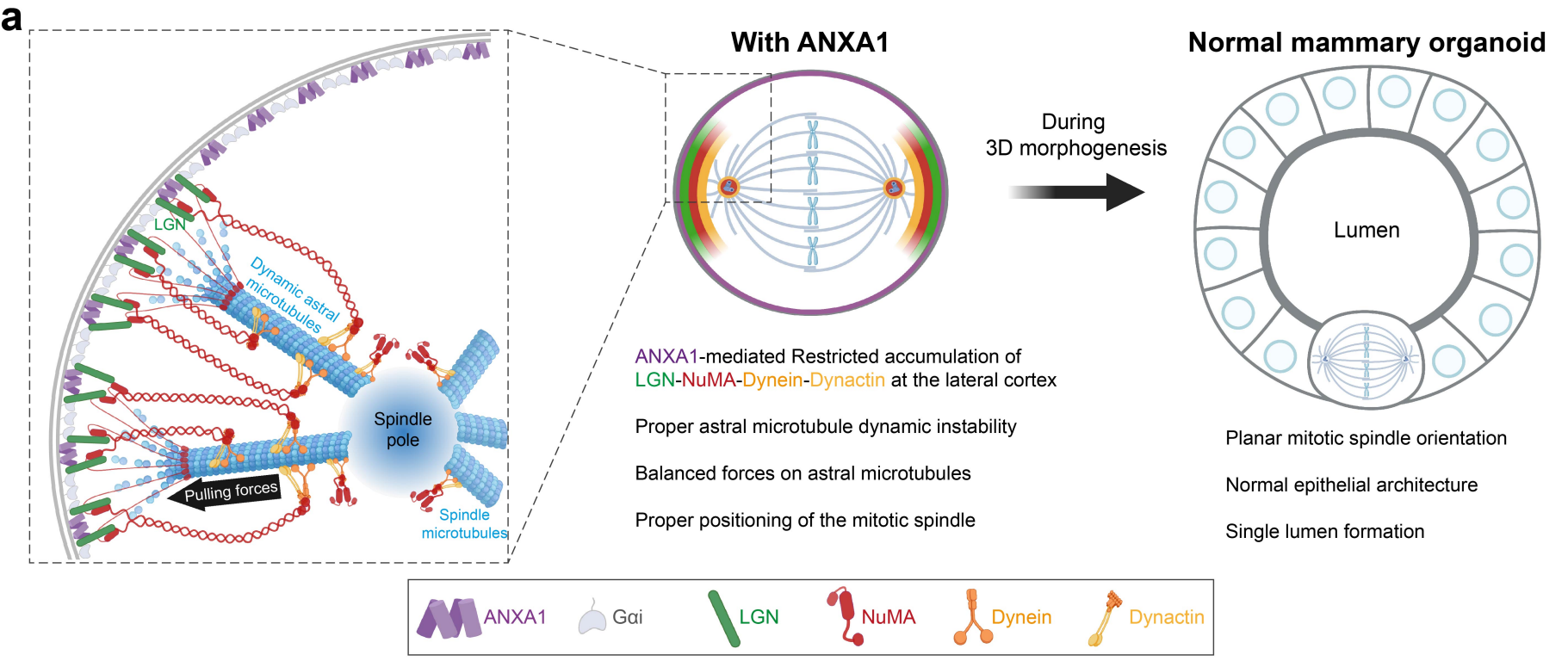

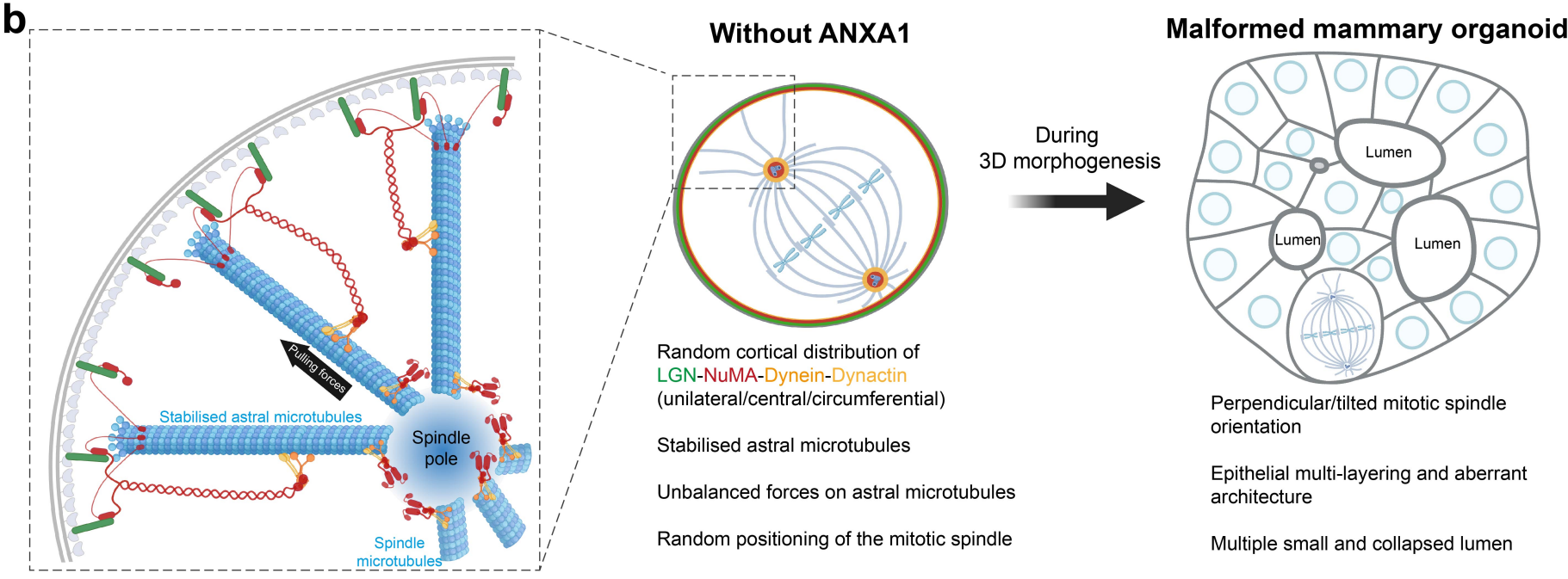

Figure 5 Proposed model for ANXA1 regulation of planar mitotic spindle orientation and epithelial morphogenesis. (a) Cortical ANXA1 interacts with LGN to instruct polarised accumulation of the LGN-NuMA complex at the lateral cortex. NuMA in turn, recruits Dynein-Dynactin generating balanced pulling forces on astral microtubules to ensure planar alignment of the mitotic spindle. During 3D morphogenesis, ANXA1-dependent regulation of planar mitotic spindle orientation is crucial for single lumen formation and normal epithelial architecture. **(b)** Loss of ANXA1 results in a diffuse cortical distribution of LGN and NuMA, which in turn impairs the recruitment of Dynein-Dynactin to the cell cortex. This affects the length and dynamic instability of astral microtubules generating unbalanced forces that result in randomised mitotic spindle orientation. During 3D morphogenesis, mitotic spindle misorientation upon ANXA1 knockdown results in epithelial multi-layering, leading to multi-lumen formation and aberrant epithelial architecture.

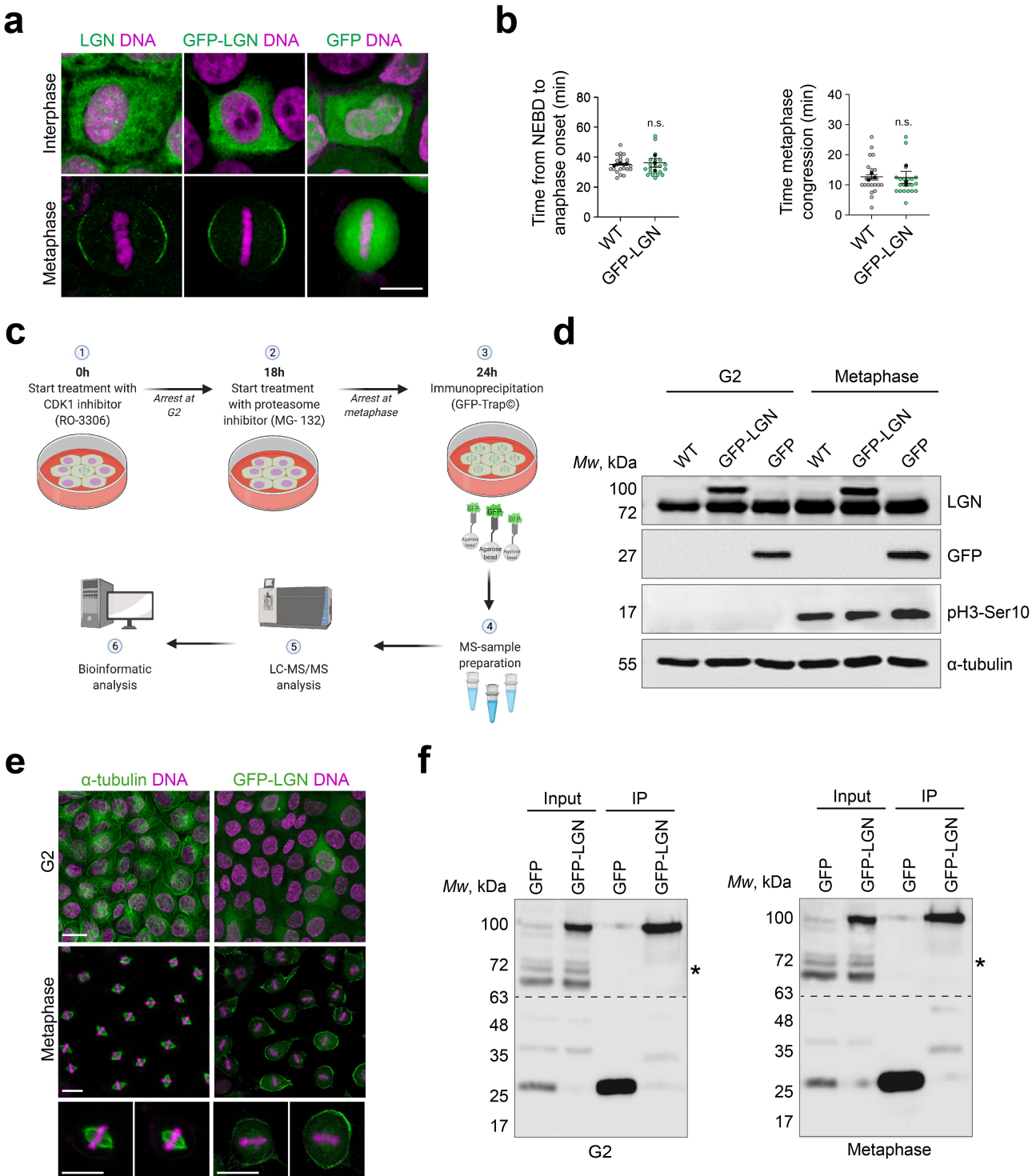
a
LGN DNA
GFP-LGN DNA
GFP DNA
Interphase
Metaphase
b
Time from NEBD to anaphase onset (min)
80
60
40
20
0
n.s.
WT
GFP-LGN
Time metaphase congression (min)
40
30
20
10
0
n.s.
WT
GFP-LGN
c
1
0h
Start treatment with CDK1 inhibitor (RO-3306)
Arrest at G2
2
18h
Start treatment with proteasome inhibitor (MG- 132)
Arrest at metaphase
3
24h
Immunoprecipitation (GFP-Trap©)
Agarose bead
4
MS-sample preparation
5
LC-MS/MS analysis
6
Bioinformatic analysis
d
G2
Metaphase
Mw, kDa
WT
GFP-LGN
GFP
WT
GFP-LGN
GFP
100
72
LGN
27
GFP
17
pH3-Ser10
55
α-tubulin
e
α-tubulin DNA
GFP-LGN DNA
G2
Metaphase
f
Input
IP
Mw, kDa
GFP
GFP-LGN
GFP
GFP-LGN
100
72
63
48
35
25
17
*
G2
Metaphase

Supplementary Figure 1 Experimental design for determining the LGN interactome in mammary epithelial cells. (a) Confocal images of representative wild type (WT) MCF-10A and the generated clonal MCF-10A stably expressing GFP-LGN or GFP in interphase and metaphase. Cells are stained for LGN or GFP (green) and counterstained with DAPI (DNA, magenta). **(b)** Time from NEBD to anaphase (left) and duration of metaphase congression (right), determined from time-lapse microscopy in WT MCF-10A cells and clonal MCF-10A stably expressing GFP-LGN (WT n = 21; GFP-LGN n = 23). **(c)** Illustration showing the proteomic workflow from the synchronisation procedure to the experimental pipeline leading to LC-MS/MS and bioinformatic-based identification of the LGN interactome. Cells were treated with the CDK1 inhibitor RO-3306, yielding cells synchronised in G2 phase, then arrested in metaphase by treatment with the proteasome inhibitor MG-132. The drugs used for synchronisation were washed out prior to extract preparation for affinity purification with GFP-Trap beads. **(d)** Western blotting of extracts from WT MCF-10A and clonal MCF-10A stably expressing GFP-LGN or GFP cells synchronised in G2 phase or metaphase. **(e)** Confocal images of representative clonal MCF-10A stably expressing GFP-LGN cells synchronised in G2 phase or metaphase. Cells are stained for α-tubulin or GFP (green) and counterstained with DAPI (DNA, magenta). **(f)** Western blotting of extracts of GFP- and GFP-LGN-bead-bound elutions from cells synchronised in G2 phase (left) or metaphase (right). Asterisks indicate endogenous LGN in the input samples. All data are presented as means ± s.e.m. from 3 independent experiments. n.s. (not significant, *t*-test). All scale bars, 10 μm.

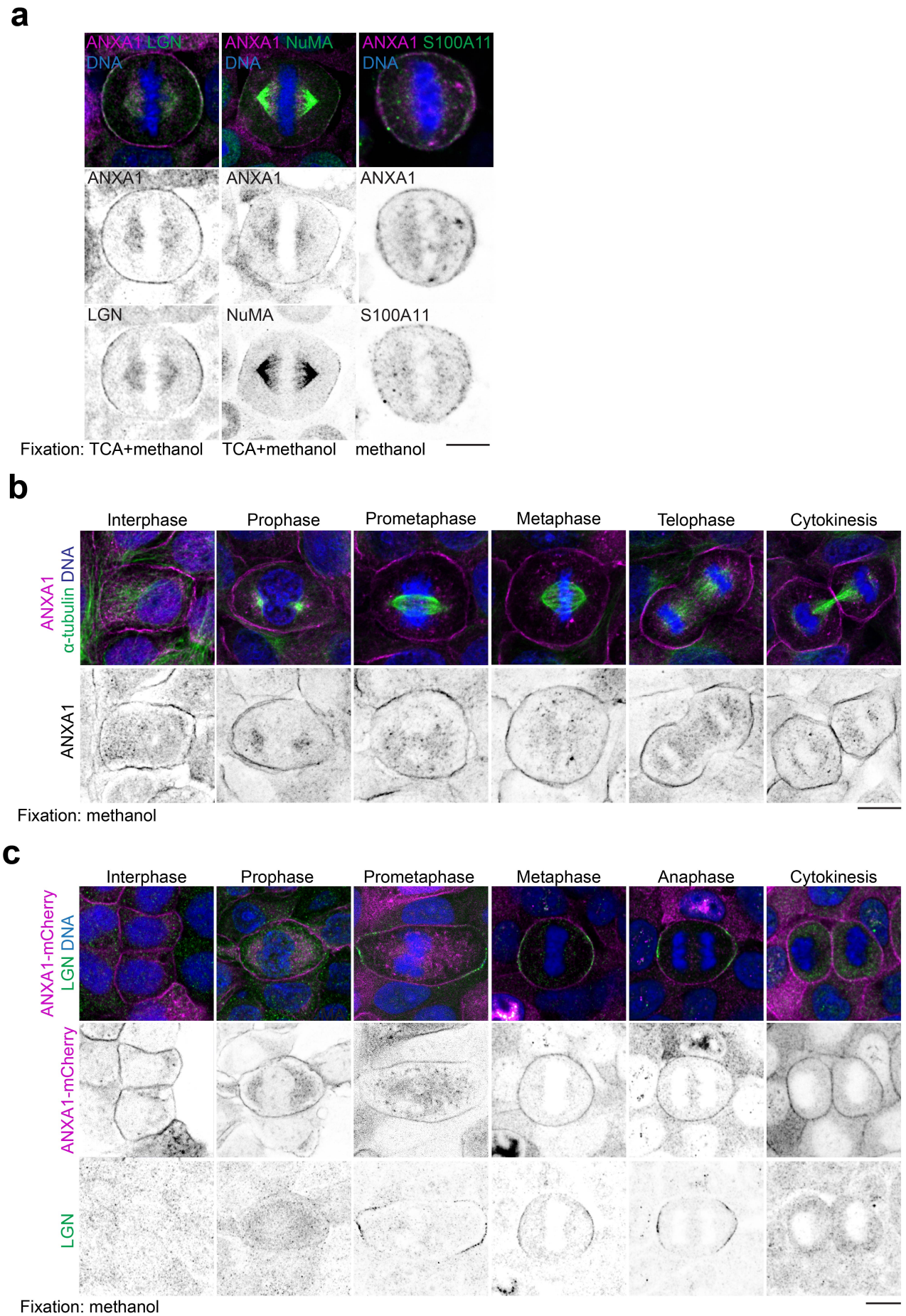
a
ANXA1 LGN
DNA
ANXA1 NuMA
DNA
ANXA1 S100A11
DNA
ANXA1
ANXA1
ANXA1
LGN
NuMA
S100A11
Fixation: TCA+methanol
TCA+methanol
methanol
b
Interphase
Prophase
Prometaphase
Metaphase
Telophase
Cytokinesis
ANXA1
α-tubulin DNA
ANXA1
Fixation: methanol
c
Interphase
Prophase
Prometaphase
Metaphase
Anaphase
Cytokinesis
ANXA1-mCherry
LGN DNA
ANXA1-mCherry
LGN
Fixation: methanol

Supplementary Figure 2 ANXA1 co-distributes with S100A11, LGN, NuMA, and microtubules. (a) Confocal images of representative MCF-10A cells stained for ANXA1 (magenta) and LGN, NuMA or S100A11 (green), and counterstained with DAPI (DNA, blue). **(b)** Confocal images of representative MCF-10A stained for ANXA1 (magenta) and α-tubulin (green), and counterstained with DAPI (DNA, blue). **(c)** Confocal images of representative clonal MCF-10A cells stably expressing ANXA1-mCherry (magenta) stained for LGN (green) and counterstained with DAPI (DNA, blue). All scale bar, 10 μm.

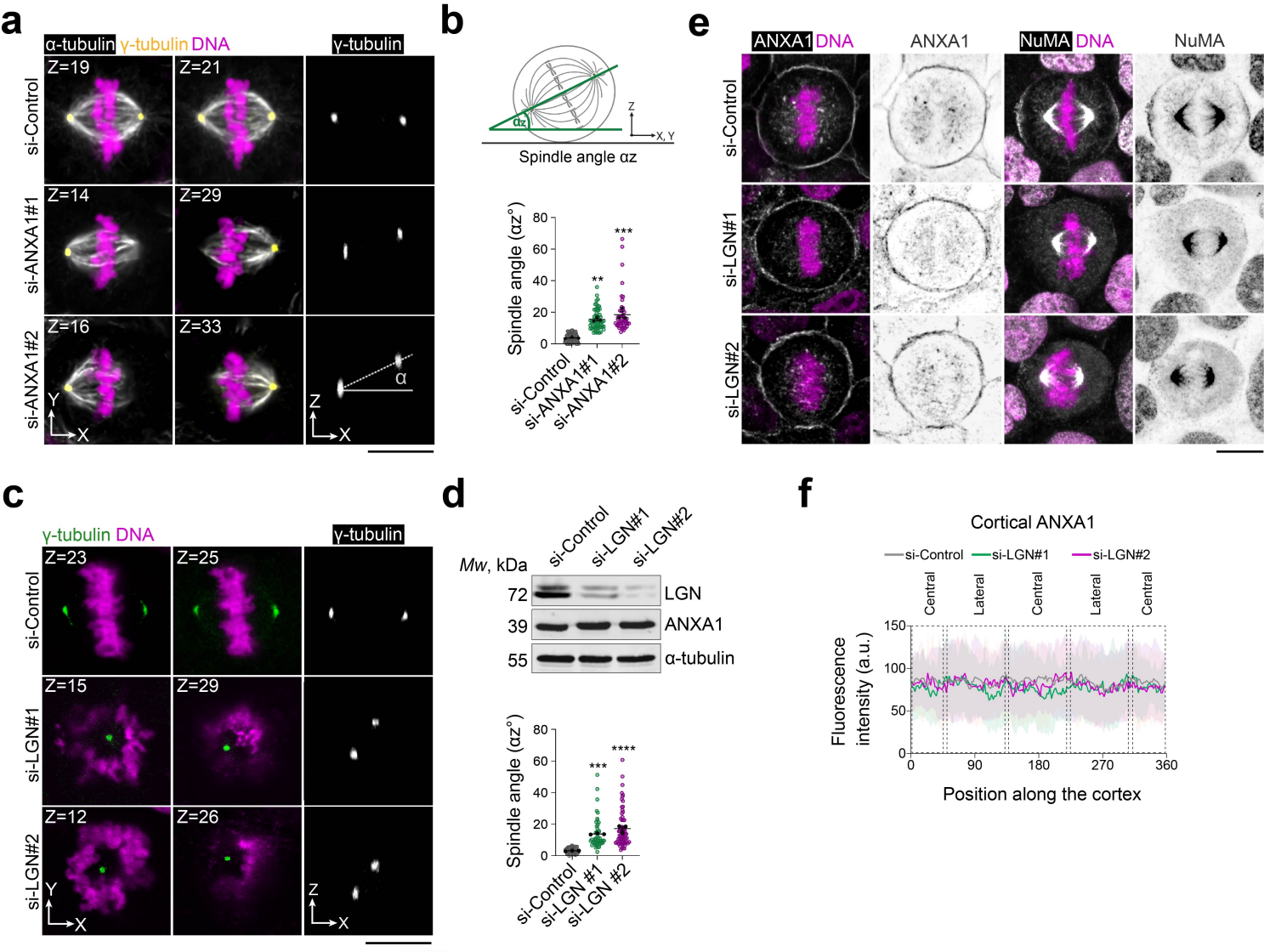
a
α-tubulin γ-tubulin DNA
γ-tubulin
si-Control
si-ANXA1#1
si-ANXA1#2
Z=19
Z=21
Z=14
Z=29
Z=16
Z=33
Y
X
Z
X
α
b
αz
Z
X, Y
Spindle angle αz
Spindle angle (αz°)
80
60
40
20
0
**
***
si-Control
si-ANXA1#1
si-ANXA1#2
e
ANXA1 DNA
ANXA1
NuMA DNA
NuMA
si-Control
si-LGN#1
si-LGN#2
c
γ-tubulin DNA
γ-tubulin
si-Control
si-LGN#1
si-LGN#2
Z=23
Z=25
Z=15
Z=29
Z=12
Z=26
Y
X
Z
X
d
si-Control
si-LGN#1
si-LGN#2
Mw, kDa
72
39
55
LGN
ANXA1
α-tubulin
Spindle angle (αz°)
80
60
40
20
0
***
****
si-Control
si-LGN #1
si-LGN #2
f
Cortical ANXA1
si-Control
si-LGN#1
si-LGN#2
Central
Lateral
Central
Lateral
Central
Fluorescence intensity (a.u.)
150
100
50
0
0
90
180
270
360
Position along the cortex

Supplementary Figure 3 ANXA1 acts upstream of LGN to ensure proper mitotic spindle orientation. (a) Confocal images of representative MCF-10A cells transfected with si-Control, si-ANXA1#1 or si-ANXA1#2 stained for α-tubulin (grey) and γ-tubulin (yellow), and counterstained with DAPI (DNA, magenta). Z projections in the XY view and XZ view are shown. Scale bars, 5 μm. **(b)** Mitotic spindle angles in siRNA-transfected cells (si-Control n = 71; si-ANXA1#1 n = 65; si-ANXA1#2 n = 49). **(c)** Confocal images of representative MCF-10A cells transfected with si-Control, si-LGN#1 or si-LGN#2 stained for γ-tubulin (green) and counterstained with DAPI (DNA, magenta). Z projections in the XY view and XZ view are shown. Scale bars, 5 μm. **(d)** Top: Western blotting of extracts from MCF-10A transfected with si-Control, si-LGN#1 or si-LGN#2. Bottom: Mitotic spindle angles in siRNA-transfected cells (si-Control n = 68; si-LGN#1 n = 50; si-LGN#2 n = 67). **(e)** Confocal images of representative MCF-10A cells stained for ANXA1 or NuMA (grey) and counterstained with DAPI (DNA, magenta). Scale bars, 10 μm. **(f)** Average cortical fluorescence intensity profiles of ANXA1 from metaphase siRNA-transfected cells (si-Control n = 41; si-LGN#1 n = 26; si-LGN#2 n = 25). All data are presented as means ± s.e.m. from 3 independent experiments. ** $P \leq 0.01$, *** $P \leq 0.001$ **** $P \leq 0.0001$ (one-way ANOVA).

Supplementary Figure 4

Fankhaenel *et al.*

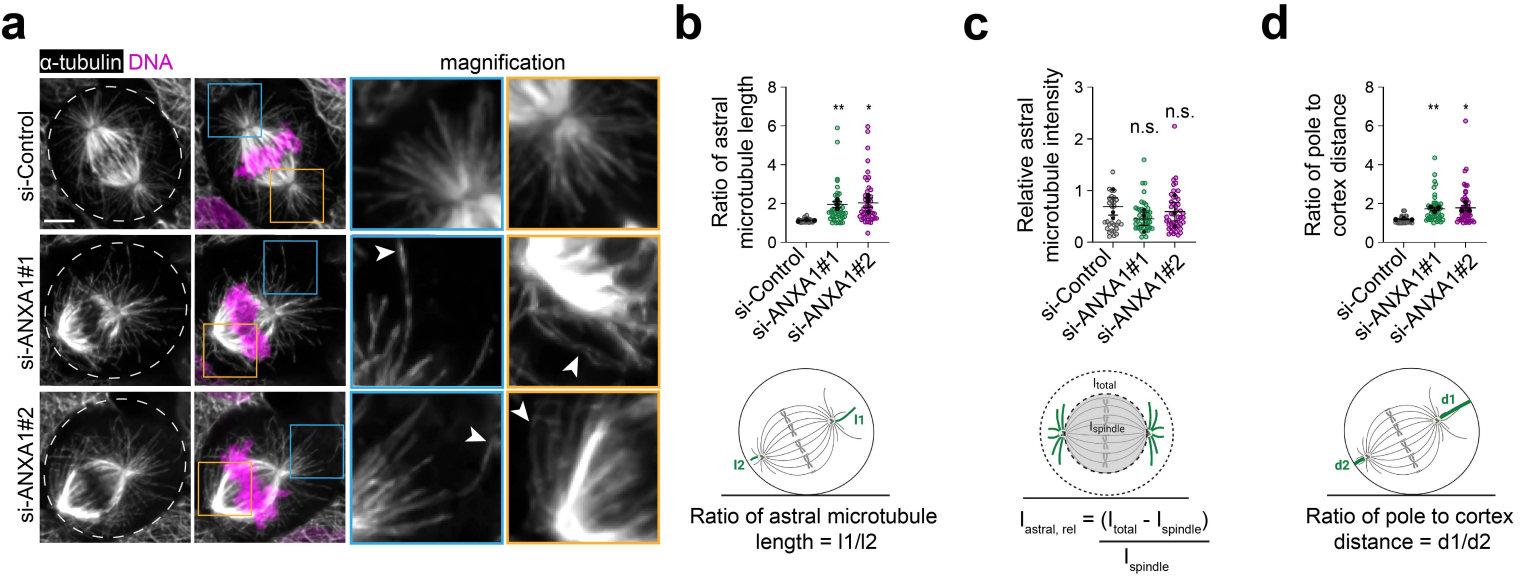

Supplementary Figure 4 Effect of ANXA1 depletion on astral microtubule length and density. (a) Confocal images of representative metaphase MCF-10A cells transfected with si-Control, si-ANXA1#1 or si-ANXA1#2 stained for α-tubulin (grey) and counterstained with DAPI (DNA, magenta). Insets show magnified images of framed regions. White arrowheads indicate elongated and buckled astral microtubules. Dashed lines outline the cell contour. Scale bar, 5 µm. **(b)** Ratio of astral microtubule length (l) in siRNA-transfected cells (si-Control n = 31; si-ANXA1#1 n = 46; si-ANXA1#2 n = 47). l1 and l2 of astral microtubules were measured as depicted on the illustration, using Fiji software. **(c)** Relative fluorescence intensities of astral microtubules ($I_{astral,\ rel}$) in siRNA-transfected cells (si-Control n = 31; si-ANXA1#1 n = 46; si-ANXA1#2 n = 47). Fluorescence intensities on the spindle ($I_{spindle}$) and total cell (I_{total}) were measured as depicted on the illustration, using Fiji software. **(d)** Ratio of pole-to-cortex distance (d) in siRNA-transfected cells (si-Control n = 31; si-ANXA1#1 n = 46; si-ANXA1#2 n = 47). Pole-to-cortex distance d1 and d2 were measured as depicted on the illustration, using Fiji software. All data are presented as means ± s.e.m. from 3 independent experiments. * $P \leq 0.05$, ** $P \leq 0.01$. n.s. (not significant), (one-way ANOVA).

Fiji custom macro for quantification of cortical protein fluorescence intensities during prometaphase

```
macro elliptic_slicing {

//number of points to measure along the cell perimeter
k=180;
//length (in pixels) of the line for each measure:
px=15;
//starting position of the scan line relative to the ellipses long axis
S=90;

titre=getTitle();
getDimensions(x,y,nb_channel,o,t);
run("Set Measurements...", "area mean standard min bounding fit redirect=None
decimal=3");
b=57.29578;
m=nResults;
IJ.deleteRows(0, m-1);
getPixelSize(unit, pw, ph, pd);
P=pd/pw;
run("Properties...", "unit=pixel pixel_width=1.0000 pixel_height=1.0000 voxel_depth="+(P)+"
origin=0,0");

		selectWindow(titre);
		run("Set... ", "zoom=150");
		setTool("Freehand");

//message prompting the user to set the ellipse:
		title = "cell center";
		msg = "use the Freehand tool to draw\n the cell's perimeter\n select the best
z-level\n then click \"OK\".";
		waitForUser(title, msg);

//measuring the ellipses center and size:
		run("Fit Ellipse");
		run ("Measure");
		x0=getResult("BX", (0));
		x1=getResult("Width", (0));
				M=getResult("Major", (0));
				m=getResult("Minor", (0));
				a=getResult("Angle", (0));
				E=sqrt(M*M-m*m)/M;
		y0=getResult("BY", (0));
		y1=getResult("Height", (0));
	//center of the ellipse:
		X0=x0+x1/2;
		Y0=y0+y1/2;

xx=newArray(k);
yy=newArray(k);
```

```
	for (i=0; i<k; i++) {
	xx[i]=(i);
	l=(360*i/k-a+S)/b;
	L=(360*i/k+S)/b;
	dia=sqrt(m*m/(1-E*E*cos(L)*cos(L)))/2;
		n1=dia-px/2;
		n2=dia+px/2;
	selectWindow(titre);
	makeLine(X0+n1*cos(l), Y0+n1*sin(l), X0+n2*cos(l), Y0+n2*sin(l));
				run ("Measure");
				yy[i]=getResult("Max", (0));
				IJ.deleteRows(0, 0);
	print(yy[i]);
	};
Plot.create("plot1", "X", "Y", xx, yy);
}
```

Supplementary Movie description

Supplementary movie 1
Description: LGN spatiotemporal distribution in control cells. Clonal MCF-10A cells stably expressing GFP-LGN were transfected with si-Control RNA for 72h and treated with Hoechst as described in the Methods. Images corresponding to 30 planes spaced by 0.6 μm through the cell volume were collected every 3 min as described in the Methods. Maximum intensity projections of GFP-LGN (green) and Hoechst (DNA, magenta) are shown through time. Time in min format and scale bar = 5 μm.

Supplementary movie 2
Description: ANXA1 knockdown impairs the dynamics of LGN and results in its unilateral distribution at the cortex. Clonal MCF-10A cells stably expressing GFP-LGN were transfected with si-ANXA1#1 RNA for 72h and treated with Hoechst as described in the Methods. Images corresponding to 40 planes spaced by 0.6 μm through the cell volume were collected every 3 min as described in the Methods. Maximum intensity projections of GFP-LGN (green) and Hoechst (DNA, magenta) are shown through time. Time in min format and scale bar = 5 μm.

Supplementary movie 3
Description: ANXA1 knockdown impairs the dynamics of LGN and results in its central distribution at the cortex. Clonal MCF-10A cells stably expressing GFP-LGN were transfected with si-ANXA1#1 RNA for 72h and treated with Hoechst as described in the Methods. Images corresponding to 40 planes spaced by 0.6 μm through the cell volume were collected every 3 min as described in the Methods. Maximum intensity projections of GFP-LGN (green) and Hoechst (DNA, magenta) are shown through time. Time in min format and scale bar = 5 μm.

Supplementary movie 4
Description: ANXA1 knockdown impairs the dynamics of LGN and results in its circumferential distribution at the cortex. Clonal MCF-10A cells stably expressing GFP-LGN were transfected with si-ANXA1#1 RNA for 72h and treated with Hoechst as described in the Methods. Images corresponding to 40 planes spaced by 0.6 μm through the cell volume were collected every 3 min as described in the Methods. Maximum intensity projections of GFP-LGN (green) and Hoechst (DNA, magenta) are shown through time. Time in min format and scale bar = 5 μm.

Supplementary movie 5
Description: Mitotic spindle and chromosome dynamics in control cells. MCF-10A cells were transfected with si-Control RNA for 72h and treated with SiR-tubulin and Hoechst as described in the Methods. Images corresponding to 30 planes spaced by 0.6 μm through the cell volume were collected every 2.5 min as described in the Methods. Maximum intensity projections of SiR-tubulin (green) and Hoechst (DNA, magenta) are shown through time. Time in min format and scale bar = 5 μm.

Supplementary movie 6
Description: ANXA1 knockdown impairs mitotic progression and results in chromosome bridges during anaphase and telophase. MCF-10A cells were transfected with si-ANXA1#1 RNA for 72h and treated with SiR-tubulin and Hoechst as described in the Methods. Images corresponding to 40 planes spaced by 0.6 μm through the cell volume were collected every 2.5 min as described in the Methods. Maximum intensity projections of SiR-tubulin (green) and Hoechst (DNA, magenta) are shown through time. Time in min format and scale bar = 5 μm.

Supplementary movie 7
Description: ANXA1 knockdown impairs mitotic progression and results in misaligned small mitotic spindles. MCF-10A cells were transfected with si-ANXA1#1 RNA for 72h and treated with SiR-tubulin and Hoechst as described in the Methods. Images corresponding to 40 planes spaced by 0.6 μm through the cell volume were collected every 2.5 min as described in the Methods. Maximum intensity projections of SiR-tubulin (green) and Hoechst (DNA, magenta) are shown through time. Time in min format and scale bar = 5 μm.

Supplementary movie 8
Description: ANXA1 knockdown impairs mitotic progression and results in misaligned multipolar mitotic spindles. MCF-10A cells were transfected with si-ANXA1#1 RNA for 72h and treated with SiR-tubulin and Hoechst as described in the Methods. Images corresponding to 40 planes spaced by 0.6 μm through the cell volume were collected every 2.5 min as described in the Methods. Maximum intensity projections of SiR-tubulin (green) and Hoechst (DNA, magenta) are shown through time. Time in min format and scale bar = 5 μm.